Injection of Graphene Oxide Nanosheets in the Brain Does not Induce Acute Neurotoxicity and Counteracts the Acute Microglial Activation related to Surgery in a Pilot Study

Corinne Portioli[1, 2, $], Cyrill Bussy[1, 3, 4 *], Mariarosa Mazza[1], Neus Lozano[1, 3], Dhifaf A. Jasim[1,3], Maurizio Prato[5,6], Alberto Bianco[7], Marina Bentivoglio[2] and Kostas Kostarelos[1,3,8, *, &]

[1] *Nanomedicine Lab, School of Health Sciences, Faculty of Biology, Medicine & Health, The University of Manchester, Manchester Academic Health Science Centre, Manchester, UK*

[2] *Department of Neurosciences, Biomedicine and Movement Sciences, University of Verona, Verona, Italy*

[3] *National Graphene Institute, The University of Manchester, Manchester, UK*

[4] *Lydia Becker Institute of Immunology and Inflammation, Faculty of Biology, Medicine and Health, The University of Manchester, Manchester Academic Health Science Centre, Manchester, UK*

[5] *Department of Chemical and Pharmaceutical Sciences, University of Trieste, 34127 Trieste, Italy*

[6] *Carbon Nanobiotechnology Laboratory, CIC BiomaGUNE, 20009 San Sebastian, Spain.*

[7] *University of Strasbourg, CNRS, Immunology, Immunopathology and Therapeutic Chemistry, UPR 3572, Strasbourg, France*

[8] *Catalan Institute of Nanoscience and Nanotechnology (ICN2), and The Barcelona Institute of Science and Technology (BIST), Campus UAB, Bellaterra, Barcelona, Spain*

[$] Current address: Neuroscience and Brain Technologies Department, Istituto Italiano di Tecnologia (IIT), Genova, Italy and Verna and Marrs McLean Department of Biochemistry and Molecular Biology, Baylor College of Medicine (BCM), Houston, TX, United States

ORCID numbers:

Cyrill Bussy: 0000-0001-8870-443X

Dhifaf A. Jasim: 0000-0002-6433-4478

Alberto Bianco: 0000-0002-1090-296X

Marina Bentivoglio: 0000-0003-4958-9795

Kostas Kostarelos: 0000-0002-2224-6672

* To whom correspondence should be addressed:

kostas.kostarelos@manchester.ac.uk ; cyrill.bussy@manchester.ac.uk

[&] Lead contact: kostas.kostarelos@manchester.ac.uk

Abstract

Carbon-based nanomaterials (CNMs) are being explored for neurological applications. However, systematic *in vivo* studies investigating the effects of CNM nanocarriers in the brain and how brain cells respond to such nanomaterials are scarce. To address this, functionalised multi-walled carbon nanotubes and graphene oxide (GO) sheets were injected in mice brain and compared with charged liposomes. The induction of acute neuro-inflammatory and neurotoxic effects locally and in brain structures distant from the injection site were assessed up to one week post-administration. While significant neuronal cell loss and sustained microglial cell activation were observed after injection of cationic liposomes, none of the tested CNMs induced either neurodegeneration or microglial activation. Among the candidate nanocarriers tested, GO sheets appeared to elicit the least deleterious neuro-inflammatory profile. At molecular level, GO induced moderate activation of pro-inflammatory markers compared to vehicle control. At histological level, brain response to GO was lower than after vehicle control injection, suggesting some capacity for GO to reduce the impact of stereotactic injection on brain. While these findings are encouraging and valuable in the selection and design of nanomaterial-based brain delivery systems, they warrant further investigations to better understand the mechanisms underlying GO immunomodulatory properties in brain.

Keywords

Graphene – carbon nanotubes – liposomes – inflammation – brain – immunomodulation - biocompatibility

Introduction

Nanomaterials may offer new solutions for unmet medical needs in the treatment of neurological disorders [1-4]. Among the different types of nanomaterials suitable for these biomedical applications, carbon-based nanomaterials (CNMs), including single-walled (SWNTs) or multi-walled carbon nanotubes (MWNTs) and graphene have recently emerged as potential new candidates given their remarkable interaction with the neural tissue [5-10]. CNMs possess unique physicochemical properties, such as high surface area, mechanical strength, electrical conductivity [11-15] and the ability to be chemically functionalised [16, 17]. In the context of neuroscience, these properties have been shown to support neuronal activity [17] and facilitate drug delivery in the brain [18, 19].

Studies performed *in vitro* have for instance revealed the promising applications of functionalised SWNTs as glutamate uptake enhancers in primary astrocytes [20] or as neuroprotective factors in primary glial cells extracted from brains of an Alzheimer's disease (AD) mouse model [21]. Similarly, in animal models, functionalised CNMs were efficient in delivering siRNA in a stroke model [22] or as drug carrier in an AD model [23]. Another step toward their clinical translation was achieved when the translocation of functionalised MWNTs (*f*-MWNTs) across the blood-brain barrier (BBB) was demonstrated, initially *in vitro* [24, 25] and then *in vivo* [26, 27]. These seminal studies have paved the way toward the targeted delivery of active therapeutics across the BBB after peripheral administration of CNMs, as proposed in one proof-of-concept *in vivo* study for brain glioma [19]. More recently, graphene-based materials (GBMs) and in particular Graphene Oxide (GO), the oxidised form of graphene that results from chemical exfoliation of graphite, have also been explored for brain therapy [6, 15]. Noticeably, GBMs were shown to inhibit the formation of β-amyloid aggregates and could thus be beneficial in preventing the progression of AD [28]. Then, chemically functionalised GO sheets were reported to be suitable photothermal platforms for destroying formed amyloid aggregates in AD model upon near-infrared light irradiation, via the generation of localised heat [29, 30]. Finally, GBMs were used as nanocarriers for anti-tumour drugs in both *in vitro* and *in vivo* models of brain cancer [18, 31], and as neurotransmission modulator with potential applications in neurobiology [32].

However, a key issue for a more widespread use of nanocarriers (including CNMs) in brain therapy is the response of the brain parenchyma once nanomaterials interact with the different cell populations of the central nervous system (CNS). This becomes especially crucial in view of potential applications of nanocarriers in brain diseases with an inherent neuro-inflammatory component, such as neurodegeneration, stroke, infection or cancer [33-35]. Therefore, to support the exploration of the full potential of CNMs for brain therapy applications, increasing effort has been devoted to investigate the possible side effects of these materials upon interaction with the brain parenchyma. MWNTs coated with polymeric material (Pluronic F127, used to increase solubility of MWNTs) were initially incubated with primary cortical neurons [36]. As these MWNTs did not induce apoptotic effects *in vitro*, their biocompatibility was then validated *in vivo* upon injection in the visual cortex of mice [36]. Similarly, no major tissue damages were reported in another study performed to analyse the neuro-

inflammation and cellular uptake of two types of *f*-MWNTs (carboxylated or amino-functionalised), after injection in the cerebral cortex [37]. Both *f*-MWNT types were internalised by microglial cells and neurons, and elicited a higher glial cell marker expression at the injection site, 2 days after injection [37]. However, at 30 days post-injection, only carboxylated MWNTs resulted in persistent glial cell activation in regions peripheral to the injection site [37]. In another set of studies, after the infusion of PEGylated SWNTs in the hippocampus of rats, an antioxidant response was observed after 24 h [38] and up to 7 days [39]. The authors theorised that the antioxidant response to SWCNTs could partly explain the moderate impact of the nanomaterials on animal behaviours [38]; moreover, the biopersistence of these CNMs at the injection site was ascribed for the persistence of the antioxidant response over 7 days [39]. Lastly, a study on the neurotoxic effect of different *f*-MWNTs using primary cultures of neuronal and glial cells derived from either the striatum or frontal cortex revealed that while *f*-MWNTs did not affect neuronal cells from any of the two brain regions or glial cells from the frontal cortex, the viability of striatum-derived glial cells decreased [40]. Although the brain region-dependent cytotoxicity to glial cells was shown to be independent of the *f*-MWNT type, it was instead associated with the number of microglial cells in the considered brain region-derived cell cultures [40], highlighting the key role of microglial cells (the resident macrophages of the brain) in the regulation of the biological response to CNMs.

More recently, the potential impact of GBMs on brain cells and tissue has also been explored. Functionalised graphene-based systems investigated as drug delivery carriers in the treatment of subarachnoid haemorrhage did not show neurotoxicity in the targeted region [41]. However, GO sheets were reported to down-regulate neuronal activity and signalling *in vitro*, albeit without affecting viability [42, 43]. Autophagy and calcium homeostasis were also found to be disturbed in neuron cultures exposed to GO, highlighting the ability of GO sheets to damage neuronal transmission and functionality, without inducing toxicity [43]. Astrocyte function and homeostasis were similarly altered by GO sheet exposure and internalisation, subsequently impacting the neuronal network that astrocytes were supporting [44]. Finally, when primary mixed glia or the microglia BV2 cell line were pre-treated with GO sheets, inhibition of NLRP3 inflammasome-dependent interleukin (IL)-1β secretion was observed upon lipopolysaccharide (LPS) and ATP priming [45].

Despite this growing knowledge and the great potential of CNMs as brain drug delivery vectors, systematic studies assessing the inflammatory potential of these nanocarriers in brain tissue remain scarce. To address this gap, three different types of engineered CNMs, including one GO type and two *f*-MWNTs (aminated or carboxylated), were here injected stereotactically into the striatum of mice and their potent inflammation was assessed. For comparison, two types of highly charged liposomes were used as benchmark drug delivery systems with previously reported tissue [46, 47] and brain [48, 49] inflammogenicity. Considering recent findings highlighting the immunomodulatory and anti-inflammatory properties of GO sheets in vitro and in vivo [32, 45, 50], the present study was also designed to test the hypothesis that GO materials present a unique inflammation profile when compared to other nanomaterials. The inflammatory potential of the different candidate nanocarriers

was therefore assessed at different time points of the acute early stage response (up to 1 week after injection) at both the molecular (i.e. transcripts encoding a panel of cytokines and chemokines) and histological (i.e. activation of astrocytes and microglial cells, number of neurons and dead cells) levels. These analyses were performed not only at the injection site (central position in the striatum) but also in adjacent and distant positions within the brain, to assess both the diffusion of inflammation processes and the delocalised effects caused by nanomaterial diffusion.

Results

Characterisation of the NMs

Either aminated or carboxylated *f*-MWNTs that have been previously explored for biomedical applications were used in the present study [22, 37, 51-54]. Their chemical functionalization is thought to not only improve solubility, but also increase biocompatibility by reducing toxicity through mitigation of the material-cell membrane interaction. The dimensional features (diameter and length) of those *f*-MWNTs were analysed by transmission electron microscopy (TEM; **Figure 1-B**, and **S1-A**). Both types of *f*-MWNTs had an outer diameter between 20 and 30 nm. Carboxylated *f*-MWCNTs (ox-MWNTs) were between 200 and 300 nm in length, while aminated *f*-MWNTs (MWNT-NH_3^+) had a length between 500 nm and 2000 nm. The Kaiser test was performed to establish the amount of amino groups present on the MWNT-NH_3^+, and found a loading of 58 µmol/g of amino functional groups (**Figure S1-A**); while the amount of carboxyl group on the ox-MWNTs had been previously determined using thermogravimetric analysis and found a loading of 1,7 µmol/g [55].

In line with our previous works, several techniques were used to assess the physicochemical properties of GO sheets (**Figures 1-B** and **S1-B**). The ζ-potential was -50.0 ± 0.4 mV. The lateral dimensions were established with TEM and were in between 10 and 1800 nm, while atomic force microscopy (AFM) revealed a thickness between 0.9 and 4.8 nm, consistent with few layer 2D materials, as we previously reported [56, 57].

Characterisation of cationic (DOTAP:Chol) and anionic (DOPG:Chol) liposomes was performed to confirm their hydrodynamic diameter size, polydispersity index (PDI) and ζ-potential (**Figures 1-B** and **S1-C**). Cationic (DOTAP:Chol) and anionic (DOPG:Chol) liposomes showed a hydrodynamic diameter of 125.6 ± 2.6 nm and 118.1 ± 3.0 nm, respectively. DOTAP:Chol liposomes showed a PDI of 0.254 ± 0.004, while in the case of DOPG:Chol liposomes, the PDI was 0.393 ± 0.061. The surface charge of the liposomes was confirmed by ζ-potential measurements. DOTAP:Chol liposomes were formed by positively charged polar chains (DOTAP, **Figure S1-C**) that attribute the cationic nature to the system (ζ= +60.5 ± 2.6 mV), while DOPG:Chol liposomes were formed by negatively charged polar chains (DOPG, **Figure S1-C**) that attribute the anionic nature to the system (ζ= -54.1 ± 0.5 mV).

Expression of inflammation-related genes

The gene expression levels of transcripts encoding inflammatory molecules were measured in the sampled brain tissue blocks. Transcripts encoding TNF-α, IL-1β, IFN-γ, IL-6 and IL-12 were used to evaluate pro-inflammatory cytokines, CCL2 and CXCL10 as pro-inflammatory chemokines, and IL-10, IL-4 and TGF-β as anti-inflammatory markers (**Table S1**).

Central brain injection site

The gene expression results for inflammatory markers in the injection site (central striatum) are presented in **Figure 2**. As expected, bacterial LPS injection (positive inflammation control) induced significantly higher expression levels for all inflammatory transcripts tested, except for *ifn-γ* mRNA at day 1 and *cxcl10* mRNA at day 1 and 2. At day 7, the upregulation of inflammatory transcripts induced by LPS was lower than at the two shorter time points, but remained significantly different from *il-10* mRNA induced by dextrose injection. Surprisingly, there was no significant upregulation of *cxcl10* expression at any time point.

In contrast, carbon nanomaterials had a limited effect on the expression levels of these genes (**Figure 2**). Over time, ox-MWNTs had a limited impact at day 1 (upregulation of *tnf-α* and *il-1β* mRNAs), high impact at day 2 (upregulation of *il-12, ifn-γ*, *il-6* and *tgf-β* mRNAs) and returned to basal levels at day 7. Similarly, GO upregulated only *tgf-β* expression at day 1, upregulated *tnf-α* and *il-6* expression at day 2, but had no effect at day 7. MWNT-NH_3^+ upregulated only the *il-6* gene at both day 1 and 2 but had no effect at day 7. Comparison of the three carbon NMs revealed that MWNT-NH_3^+ had the safest inflammatory profile at day 1 while GO was the safest at day 7. At day 2, both MWNT-NH_3^+ and GO behaved similarly, while ox-MWNTs induced the greatest inflammation.

Liposomes were used here as positive nanomaterial controls and were found to more broadly affect gene expression (**Figure 2**). DOTAP:Chol upregulated *il-6* and *il-10* mRNAs at day 1; this upregulation persisted at day 2, when expression levels of *tnf-α*, *il-1β* and *tgf-β* mRNAs were also upregulated. In addition, the inflammation induced by DOTAP:Chol was maintained at day 7 with upregulation of *ifn-γ*, *ccl2* and *cxcl10* gene transcripts. Similarly, DOPG:Chol upregulated *il-12*, *il-6* and *il-10* mRNAs at day 1 and upregulated *tnf-α*, *il-1β*, *il-12*, *il-10* and *ccl2* expression at day 2 but returned to basal level at day 7. When comparing the two types of liposomes, no significant differences were observed for any inflammatory marker at day 1. At day 2, significant differences were found for ccl2 mRNA only. At day 7, significant differences were found for *tnf-α*, *ifn-γ*, *il-12*, *ccl2* and *cxcl10* mRNAs, revealing an accentuated pro-inflammatory profile for cationic DOTAP:Chol liposomes in comparison to anionic DOPG:Chol liposomes.

Among the different NMs, carbon NMs appeared to elicit the mildest inflammatory response at the injection site. Both MWNT-NH_3^+ and GO yielded similar results, whereas ox-MWNT was the most pro-inflammatory NM, especially at day 1 and 2 post-injection.

Adjacent posterior brain region

The results of gene expression for different inflammatory markers in the posterior brain region in direct contact with the injection site are presented in **Figure S2**. After LPS injection, upregulation of transcript levels for all markers followed the same trends as in the site of injection. At day 1 and 2, all transcripts were upregulated except for *ifn-γ* mRNA at day 1. At day 7, expression of the *tnf-α* and *il-1β* genes were still upregulated.

At day 1, carbon NMs had no significant impact on the expression of any of the genes tested in this brain region (**Figure S2**). At day 2, all three carbon NMs regardless of their characteristics significantly downregulated *tnf-α* expression and upregulated *ccl2* expression. At day 7, none of the carbon NMs had any significant effect. No significant differences were observed at any time point among the three carbon NMs, despite a trend suggesting a mild (compared to nanotubes) inflammatory profile after GO administration, especially at day 7 (*i.e. ccl2*, *il-12*, and *ifn-γ* mRNAs had lower values, albeit without statistical significance).

In contrast, following injection of liposomes, DOPG:Chol significantly upregulated *ccl2* and *cxcl10* mRNAs at day 1, whereas DOTAP:Chol had no effect in the posterior brain region (**Figure S2**). At day 2, while DOTAP:Chol significantly upregulated *il-1β* and *il-10* transcripts, DOPG:Chol upregulated *tnf-α* and *ccl2* mRNAs. At day 7, none of the liposomes had any effect on inflammatory marker gene expression, highlighting the transient inflammatory impact of these materials, possibly due to their well-known poor long-term structural stability in living tissue.

Distant anterior brain region

Gene expression levels for the inflammatory markers in the anterior brain region (distant from the injection site) are presented in **Figure S3**. As described above, at day 7 in the posterior brain region (in direct contact with the injection site), a drastic decrease of the inflammatory response for all markers and conditions tested was observed, including LPS injection (**Figure S2**). We therefore reasoned that in a distant brain site (not in direct contact with the site of injection) inflammation levels at day 7 would be even lower. This led us to investigate gene transcripts in the distant anterior brain region only at day 1 and 2 (**Figure S3**). A second motivation for performing analyses of gene transcripts in the anterior striatum after injection in the middle/central striatum (these two parts of the striatum being at relative distance from each other) was brought about the hypothesis that liposomes can diffuse across this brain region and therefore induce inflammation beyond the site of injection [58, 59]. In addition, analyses were performed only for liposomes, as they were inducing upregulation of genes in the posterior brain region (**Figure S2**), whereas all carbon NMs did not induce any gene upregulation in this brain region (**Figure S2**).

The results following LPS injection in the anterior brain region were identical to those found for the posterior brain region at day 1 and 2, with an upregulation of all markers except for *ifn-γ* expression at day 1 (**Figure S3**). At day 1, anionic DOPG:Chol liposomes elicited the greatest inflammatory

response, with significant upregulation of *tnf-α*, *il-1β*, *il-6*, *ccl2* and *cxcl10* mRNAs, whereas cationic DOTAP:Chol only upregulated *il-1β* expression. In contrast, DOTAP:Chol liposomes were more inflammatory at day 2, with upregulation of *tnf-α*, *il-1β*, *ccl2* and *cxcl10* expression, while DOPG:Chol liposomes only upregulated *il-12* expression.

Overall, anionic DOPG:Chol liposomes seemed to have a greater inflammatory potential at day 1 and 2 not only at the injection site but also in nearby and distant regions of the brain. In contrast, cationic DOTAP:Chol liposomes showed a greater inflammatory potential at day 2 in all brain regions, persisting at day 7 only in the site of injection. These results suggested that liposomes, as hypothesised, can diffuse across the brain tissue from the injection site and mediate pro-inflammatory effects along their path.

Impact on microglial cells and astrocytes

To investigate the effect of the tested NMs on microglial cells and astrocytes, we focused our efforts on day 2. This time point was selected based on the molecular findings presented above, which indicates that expression levels of pro-inflammatory transcripts were higher 2 days after injection than at the other time points. The same three brain regions assessed for the RT-qPCR analyses were used for the histology study (**Figure 1-A**).

Glial cell analyses were based on CD11b and GFAP immunophenotyping. Both qualitative observations of cell features to detect structural changes indicating an activated state (such as cell body hypertrophy and increased thickness of processes) and quantitative analyses were performed (CD11b, **Figure 3 -Ai**, **-Bi**, and **-Ci**; GFAP, **Figure 3 -Aii**, **-Bii**, and **-Cii**). The latter evaluated the following different parameters: *i)* area covered by microglia and astrocytes, including cell branches (a higher area indicating cell hypertrophy) (**Figures S4-A** and **S5-A**), *ii)* intensity of microglial cell immunoreactivity evaluated by densitometry (increased intensity indicating CD11b upregulation) (**Figure S4-B**) and *iii)* astrocyte cell number (an increased cell number indicates astrocytic activation) (**Figure S5-B**).
The area covered by microglial cells (**Figure 3 -Ai**, **-Bi**, and **-Ci**) and astrocytes (**Figure 3 -Aii**, **-Bii**, and **-Cii**) was evaluated for all conditions tested and in the three brain regions considered. The analysis was also conducted in matched regions of the contralateral hemisphere to obtain data in tissue devoid of mechanical trauma due to stereotactic injection or surgery.

Microglial cells

Immunolabelled microglial cells at the injection site did not show features of activation, or only mild activation in comparison to vehicle control (5% dextrose in water), at day 2 after injection (**Figures S4-A** and **3-Bi**). This was observed for all NMs and doses tested here. Only injection of cationic DOTAP:Chol or anionic DOPG:Chol liposomes replicated the features observed after LPS injection (*i.e.* hypertrophy and “bushy” appearance of microglial cells). However, this was not significantly different from the vehicle control, as analysed quantitatively (**Figure 3-Bi**). High cell death, likely

involving both neurons and glia, was observed at the site of injection after either of these liposomal treatments and could account for this finding. Surprisingly, GO injections at 1 mg/ml resulted in significantly lower CD11b immunoreactivity than control vehicle injection and was similar to that observed in the contralateral non-injected hemisphere (**Figure 3-Bi**). Administration of either type of *f*-MWNTs at both 0.5 and 1 mg/ml and GO at 0.5 mg/ml induced a glial cell activation comparable to that observed after vehicle injection.

In brain tissue sections distant from the injection site (i.e. anterior brain region), weak microglial cell activation was observed after NM injections, while LPS induced clear microglial cell activation (**Figure S4-A**). When analysed quantitatively and in comparison to the contralateral region, only LPS injection elicited a significant activation of CD11b-positive cells (**Figure 3-Ai**). All the other conditions, including both types of *f*-MWNTs or liposomes and GO, induced microglial cell activation at a level similar to that induced by vehicle injection or even lower, and was similar to that observed in the contralateral hemisphere. Only cationic DOTAP:Chol liposomes (and to a lesser extent DOPG:Chol liposomes) induced microglial cell activation that was slightly more pronounced (but not significant) than the vehicle.

In sections from brain tissue in direct contact with the injection site (i.e. posterior brain region), mild activation of microglial cells was observed after injection of LPS and anionic DOPG:Chol liposomes; this was also observed to a lesser extent after cationic DOTAP:Chol liposome injection (**Figure S4-A**). Accordingly, quantitative evaluation of the percentage of the area covered by CD11b-positive cells showed a significant increase only in brains after LPS or DOPG:Chol liposome injection (**Figure 3-Ci**). DOTAP:Chol injection induced a modest, but not significant, increase of CD11b-positive cell coverage compared with both vehicle control injection and the contralateral region. Both types of *f*-MWNTs at either concentration had no effect on activation of microglial cells in this region with results similar to vehicle control injection. Noticeably, GO injection at either concentration resulted in a lower signal than the vehicle and was more comparable to the contralateral region, albeit not significantly.

Based on these results, particularly the surprising results obtained with GO *versus* liposomes or *f*-MWNTs, a densitometric evaluation of CD11b immunostaining intensity was performed in brain sections containing the injection site and compared against results obtained from LPS- and vehicle-injected brain tissues (**Figure S4-B**). Consistent with the findings mentioned above, densitometric analysis revealed a significantly lower CD11b optical density after administration of GO than after vehicle, at the two tested GO doses. These results suggest that the presence of GO could be beneficial in reducing the trauma of surgical injection in the striatum. In contrast, and as expected, CD11b optical density after LPS injection was significantly higher than vehicle injection. Differences in this parameter between injection of DOTAP:Chol or DOPG:Chol liposomes and vehicle were not significant.

Astrocytes

Hypertrophic astrocytes, as indicated by higher GFAP immunoreactivity, were observed after LPS injection at the injection site (**Figure S5-A**). Accordingly, the relative surface area covered by astrocytes after LPS injection showed a significant increase when compared with vehicle control injection (**Figure 3-Bii**). Although not significant, the area covered by GFAP-positive cells was also slightly increased after injection of ox-MWNT at both concentrations or injection of anionic DOPG:Chol liposomes when compared with vehicle. None of the other NMs induced significant differences when compared with vehicle control injections, but all conditions induced higher astrocyte coverage than in the matched, contralateral non-injected brain regions; this suggests that the mechanical trauma due to their respective injections could account for this mild astrocytic reaction.

In brain sections from the anterior region (distant from site of injection), mild features of astrocyte activation were observed after administration of LPS or cationic DOTAP:Chol liposomes (**Figure S5-A**). Accordingly, the relative surface area of the brain tissue covered by GFAP immunoreactivity was significantly higher after injection of LPS and DOTAP:Chol liposomes than after vehicle, although values were lower after injection of DOTAP:Chol than LPS (**Figure 3-Aii**). None of the other NMs induced significant differences. Although not significant, values were lower after GO injection than after vehicle injection (for both GO doses tested) and were similar to the contralateral hemisphere, consistent with the results for microglial cell reactivity after GO treatment. For all conditions, the relative surface area of the tissue covered by GFAP immunoreactivity was overall lower in this anterior brain region than at the injection site (**Figure 3-Aii** and **-Bii**).

In the posterior brain region (*i.e.* sections in close vicinity to the injection site), astrocyte activation was observed only after LPS injection and to a far lesser extent after DOTAP:Chol or DOPG:Chol liposome injection (**Figure S5-A**). Astrocytes had normal appearance for every other condition. These observations were supported by quantitative evaluation of the area covered by GFAP immunoreactivity (**Figure 3-Cii**). Only LPS induced a significant increase of GFAP coverage. Values after DOTAP:Chol or DOPG:Chol liposome injection were slightly higher than after vehicle administration, while every other condition showed values similar to or lower than vehicle-injected controls. Noticeably, values after GO at 1 mg/ml were lower than after vehicle injection and similar to those in the matched contralateral brain region.

Considering these results and the higher astrocyte activation observed in the anterior brain region after injection of cationic DOTAP:Chol liposomes, astrocyte cell number was analysed after injection of DOTAP:Chol liposomes and compared to both positive (LPS) and negative (vehicle) controls (**Figure S5-B**). DOTAP:Chol liposome injection did not significantly affect the number of astrocytes in the three analysed brain regions, despite being higher than the vehicle control in the anterior brain region. The latter result was concordant with the relative coverage of GFAP-positive cells in DOTAP:Chol liposome-injected brains (**Figure 3**), which showed greater astrocyte activation than after vehicle injection but lower than after LPS injection. Astrocyte number was also significantly

increased in the anterior and posterior brain regions after LPS injection, but was not significantly increased in the injection site. These findings were also in agreement with the relative coverage of GFAP-positive cells that showed that LPS resulted in higher values in both the anterior and posterior brain regions (**Figure 3-Aii** and **-Cii**) than in the injection site (**Figure 3-E**) when compared with vehicle. As mentioned above, this could be explained by the high cell death (involving glia) elicited by LPS in the injection site (**Figure 3-Bii**).

Impact on neuronal cell viability

Akin to glial cells, the impact of the different NMs on neurons was also studied at day 2 after injection. Neuronal cell death following injection of NMs was quantified using NeuN immunostaining (**Figure S6**). Statistical evaluation was performed by comparing each data set with that obtained after vehicle injection in the respective brain region (**Figure 3 -Aiii**, **-Biii**, and **-Ciii**). Only in the injection site and after LPS or cationic DOTAP:Chol liposome injections was a significant loss of neurons observed (**Figure 3-Biii**). LPS induced higher neuronal cell loss compared to DOTAP:Chol. No significant neuronal cell loss was observed after injection of the other NMs or in the other two brain regions.

Based on neuronal cell loss, the number of apoptotic cells were analysed measuring the cleaved caspase 3 immunoreactivity after LPS and cationic DOTAP:Chol liposome injections, and were compared to vehicle and GO injections (**Figure 4**). The greatest number of cleaved caspase 3 positive cells was found in brain sections containing the injection site after LPS or cationic liposome injections, in agreement with the loss of NeuN immunoreactivity. Interestingly, a greater number of cleaved caspase 3 positive cells was also observed in the cerebral cortex at the level of the injection site, possibly associated with the needle track passing through the cortex to reach the striatum, but only after LPS and DOTAP:Chol liposome injections and not after vehicle or GO injections. This suggests a safer toxicological profile for GO than DOTAP:Chol liposomes, consistent with the results obtained with CD11b immunoreactivity (**Figure S3-B**).

Finally, a Fluoro-Jade B staining was performed (**Figure S7**) to label neurons undergoing degeneration [60]. Combining Fluoro-Jade B staining with cleaved caspase 3 staining would help confirming whether cleaved caspase 3 positive cells were in fact neurons. Consistent with both the NeuN and cleaved caspase 3 signals, only LPS-injected brains had Fluoro-Jade B labelled neurons in the striatum. In the cortical tissue surrounding the needle track, a limited number of Fluoro-Jade B positive cells were observed after injection of LPS, DOTAP:Chol liposomes, or (to a lesser extent) vehicle. Surprisingly, no Fluoro-Jade B stained cells were observed after GO injection in the striatal or cortical regions, suggesting that the presence of GO sheets may have prevented the brain tissue damages associated to surgery and observed after vehicle injection, which supports the data obtained with CD11b immunoreactivity (**Figure S4-B**). Results from NeuN and cleaved caspase 3 immunostaining clearly revealed that NMs inducing neurotoxicity (*i.e.* DOTAP:Chol liposomes) were only detrimental at the site of injection, but not in adjacent brain regions. This finding was suggesting

that, despite the potency of these materials to diffuse across the brain tissue (as indicated by their inflammatory potential across the three tested regions), the amount of diffusing materials is likely to be limited, or that neurotoxicity requires a high dose of materials, such as found at the injection site, to occur.

Taken together, the results obtained with NeuN, cleaved caspase 3 and Fluoro-Jade B indicate that only cationic DOTAP:Chol liposomes (and the positive control for inflammation, LPS) had a clear negative impact on cells and primarily at the site of injection. In contrast, GO appears to have a safer and potentially beneficial profile in respect to neurons.

Discussion

Due to their unique properties and dimensions, engineered nanomaterials have emerged as novel nanomedicine solutions for the treatment or diagnosis of various neurological conditions [1]. However, the CNS is a very sensitive environment. If freely bioavailable in the brain parenchyma, nano-sized foreign materials such as nanocarriers may easily cause disruption to physiological processes and functions. It is therefore of greatest importance that safety considerations are implemented at an early stage during the development of biomedical nanomaterials for CNS applications [61]. For this to happen, a better understanding of the nanomaterial physicochemical characteristics that may induce adverse effects in the brain, such as inflammation, is warranted. This is particularly essential for biomedical nanomaterials developed to treat brain diseases that already have an inflammatory component [34, 35].

Recently, both carbon nanotubes and graphene-based materials have shown great promise for the treatment and imaging of neurological disorders. However, there is a limited number of studies that have specifically explored the neuro-inflammation profiles of these CNMs in the brain. With this in mind, we went on investigating the neuro-inflammatory potential of different CNMs that could potentially be used as brain nanomedicines. The tested nanocarriers were directly injected in the striatum, which was used here as a model of centrally positioned brain region for assessing the reactions of the three main cell types of the brain (namely neurons, astrocytes, and microglial cells) to exogenous materials. Along with CNMs, both cationic and anionic liposomes were used as benchmark materials with known inflammatory properties in various tissues [46, 47] or the brain [48, 49, 62]. These inflammatory properties are due to their high density of surface charges. Indeed, while anionic micelles were shown to be well tolerated regardless of administration modalities [48], cationic micelles and cationic liposomes elicited immune cell infiltration and neuronal degeneration due to inflammatory response after central administration [48, 49].

In the present study, the inflammatory potential of the different nanomaterials was then tested at both molecular and histological levels. These investigations were performed not only in the area of the brain injected with the candidate nanocarriers, but also in adjacent brain areas, either in close vicinity to the

site of injection (*posterior area*) or a few mm away from the site of injection (*anterior area*). This assessment in three different locations of the same striatum was designed to assess the possible diffusion of the materials or biological effects (or both) across the injected brain region, namely the striatum. In addition, different doses of nanomaterials were considered. The main tested dose for *f*-MWNTs and GO (*i.e.* 0.5 µg) was based on previous studies for drug delivery purposes using similar administration route, bypassing the blood brain barrier [22, 53]. This amount was then doubled to directly compare with the dose used for liposomes and to assess the role of positive and negative charges in the inflammation profile of surface-charged CNMs, such as functionalised MWNTs and GO. All tested materials were compared to a negative control, an injection with the vehicle (5% dextrose in water), which reflected the background inflammatory response to the brain tissue damage induced by the stereotactic surgical procedure. The reported neuro-inflammation profiles for the different nanomaterials tested are therefore representing not only the brain tissue response to the material injections, but also how each tested nanomaterial modulated the inflammatory response inherent to the brain surgery used to administer those materials [50]. NM treatments were also compared to LPS, a known inflammogenic compound.

Gene expression analyses of pro- and anti-inflammatory markers revealed that the tested nanomaterials elicited different patterns of inflammatory response in the considered brain areas. In general, regardless of their nature, the levels of pro-inflammatory markers after the administration of nanomaterials were found to be significantly lower than those elicited by LPS injection at days 1 and 2, when the LPS-induced upregulation was greatest. But an overall mild acute neuro-inflammatory response was found for all the different nanomaterials tested, in comparison to the negative control. Although the administration of carbon NMs, including GO, elicited a mild upregulation of pro-inflammatory transcripts immediately after injection, still observable at day 2, gene expression levels for these materials were comparable to the negative control by day 7. These findings are in agreement with previous investigations in which *f*-MWNTs that were either carboxylated and aminated or aminated only, had been injected in the cerebral cortex of mice and induced in both cases a transient inflammatory reaction, attributed to both nanomaterial and brain surgery, with brain tissue showing no signs of inflammation by day 14 [37]. Contrastingly, injection of cationic liposomes induced marked levels of transcripts encoding pro-inflammatory markers (particularly at the site of injection) that persisted for up to 7-day after injection, in agreement with previous studies [48, 49].

In brain regions close to (but not within) the injection site, there was an overall lower level of pro-inflammatory transcripts compared to the injection site. Apart from day 2, the administration of *f*-MWNTs and GO did not elicit upregulation of any pro-inflammatory mediators in a nearby brain region from the injection site, which is consistent with a previous study that did not reveal any diffusion of the biological effects after intra-cerebroventricular injection [37]. However, despite the distance from the injection site, the administration of cationic liposomes induced marked upregulation of inflammatory markers in these brain regions at both day 1 and 2. This suggests potential diffusion of either the biological response via intercellular signalling, possibly mediated by activated microglial

cells, or the nanomaterials (or both). This observation is consistent with observations by Knudsen *et al.* [48]. In this study, macrophage infiltration was observed both in the injection site and in a nearby brain region 1 week after the injection of cationic and anionic liposomes in the dentate gyrus of rats.

Neurotoxicity leading to neurodegenerative effects represents a major concern for the use of nanocarriers in the brain [54]. The results obtained in the present study did not reveal acute neuronal cell death effects for most of the analysed nanomaterials. Indeed, cell counting revealed a significant decrease of neuronal cell number in the injection site only after administration of cationic liposomes. These findings are consistent with results obtained in a previous study in which the potential systemic and central toxic responses were evaluated after brain administration of non-PEGylated cationic (DOTAP:Chol-Chol) liposomes or PEGylated micelles that were either cationic or anionic [48]. In the latter study, intra-cerebroventricular administration of cationic liposomes induced inflammatory cell infiltration, neuronal degeneration, and cell apoptosis, whereas the administration of anionic particles did not cause any toxic reaction [48]. Similarly, in the present study, the DOPG:Chol anionic liposomes did not induce neurotoxicity, while cationic DOTAP:Chol liposomes resulted in neurotoxic effects. However, while LPS elicited glial and neuronal cell death at the site of injection, cationic liposomes only affected neuron cell number. This could be due to the properties of cationic liposomes, which are instable nanosystems characterised by rapid clearance due to fusion with cell membranes, hence are short-lived [63].

In contrast to liposomes, regardless of their surface charge none of the CNMs induced neurotoxicity. This is consistent with a previous long-term (12 w or 1 y) experimental study on brain tissue response following the injection of nanowires with different lengths (2, 5, and 10 μm) in which no significant differences in the number of neurons were measured [59]. In another study, PEGylated SWNTs did not induce cerebral tissue damage or cognitive function alterations at 1 or 7 days after infusion in the rat hippocampus [39]. In addition, despite short-term oxidative damage observed at 30 min, an unanticipated antioxidant effect was observed after 7 days, suggesting a potential neuroprotective ability of these functionalised carbon nanotubes [39].

The brain inflammatory response to nanocarrier injection is expected to be mediated by glial cells, since both microglia and astrocytes act as scavengers for maintaining homeostasis and signalling between cells. On one hand, astrocytes control ion and nutrient balance [64], and are activated upon injury, which manifests structurally by an hypertrophy of the cell body and processes, and an upregulation of GFAP [65]. On the other hand, microglial cells are the main CNS immune-resident components, reacting to early changes in neuronal activity or to pathological conditions [66] and constitute the main defence mechanism in the brain. Therefore, the responses of both microglial cells and astrocytes were analysed in detail in the present study.

At the injection site, no activation of microglial cells was observed after injection of CNMs, regardless of their type or surface charge, whereas hypertrophic microglial cells were observed after injection of

liposomes (also regardless of their surface charge). Interestingly, in the brain region adjacent to injection, mild microglia activation was observed after administration of both positively-charged amino *f*-MWNTs and liposomes (anionic or cationic). These findings are consistent with a previous study in which a local inflammatory response was induced by *f*-MWNTs [37]. In addition, a mild astrocyte response was observed here at the injection site 2 days after injection, particularly after administration of ox-MWNTs and anionic liposomes. In adjacent or distant brain regions, the astrocyte response was significantly lower with respect to the injection site. A previous *in vitro* study, performed on primary mixed glial cell cultures, emphasised the importance of microglial cells and how their number (with respect to other cells such as astrocytes) can affect biological outcomes [40]. We observed that administration of cationic liposomes induced astrocyte activation at a distance from the injection site, consistent with the pro-inflammatory gene expression response observed in the same brain region with RT-qPCR analyses. These findings agree well with results obtained in a previous study in which both astrogliosis and microgliosis (based on GFAP and Iba1 immunostaining) were identified directly at the site of injection of cationic micelles or in nearby brain regions [48]. In contrast, anionic micelles did not induce a similar activation, highlighting the safer profile of negatively charged nanomaterials when compared to positively charged nanomaterials. Indeed, anionic particles interact less with cell membranes that are negatively charged surface. In contrast, cationic particles, due to a higher electrostatic interaction with negatively charged cells, can accumulate to a greater extent in cells and create a more significant burden. This in turn increases the potential of positively charged nanomaterials to exert a toxic effect [67, 68].

Regarding the overall brain inflammation potential of the different nanomaterials tested here, GO nanosheets appeared to have the least inflammatory profile, when combining both molecular and histological results. This is consistent with a recent review that mentioned that, thus far, graphene-based nanomaterials (including GO) appear to be safer than carbon nanotubes [69]. When comparing carbon nanotubes and carbon based two-dimensional lattices, not only the dimensions (lateral, thickness or length) but also physicochemical features such as rigidity/stiffness or bioavailable surface area could be amongst the explanatory material factors making GO more tolerable than MWNTs under the tested conditions [70, 71]. However systematic investigations addressing those questions and comparing the two types of materials are lacking so far, in both the nanotoxicology and nanomedicine literatures. Here, we observed that GO nanosheets not only induced a moderate and acute inflammatory response (*tgf-β* over-expressed at day 1; *tnf-α* and *il-6* over-expressed at day 2; expression levels similar to negative control for all transcripts by day 7), but also led to a lower level of glial cell activation at day 2 when compared to vehicle injection (i.e. glial activation due solely to surgery in this later case), especially at the 1 mg/mL dose. In addition, GO induced less neurotoxicity than LPS, cationic liposomes, or even the vehicle control. This suggests that the presence of GO in the brain could be beneficial to reduce the impact of intra-parenchymal stereotactic surgical injection of materials, a traumatic injury that causes inflammation and cell death by itself, as evidenced in the negative control results reported here. These findings are consistent with a study [50] that reported that mouse brain directly injected with GO had lower GFAP

immunoreactivity at 48 h and lower iba1 immunoreactivity at 72 h after injection compared to negative vehicle control, suggesting that GO had the capacity to lower the activation of astrocytes and microglial cells, both caused by the brain surgery at the injection site. In agreement with this, another study reported the immunomodulatory effects of GO pre-treatment on the macrophage response to inflammatory challenge [45]. In this study, GO pre-treatment had an anti-inflammatory effect upon activation of the inflammasome. Specifically, GO sheets reduced the release of IL-1β and IL-6 by an NRF2-mediated mechanism. This effect was observed not only in immortalised bone marrow-derived macrophages but also in a primary murine mixed glia and immortalised microglia BV2 cell line. While all these converging findings, including ours, are encouraging from a biomedical perspective, they warrant further investigations to fully understand the underlying mechanism of the immunomodulatory effects of GO nanosheets. In particular a greater sample size, a broader range of doses and longer time points after injection will be required to reveal how these effects could be controlled and safely translated into valuable clinical applications of GO based nanovectors for brain diseases.

Conclusion

In the present pilot study looking at the acute response to injection of nanovector candidates in the brain, lipid-based NPs, particularly cationic liposomes, induced the greatest inflammatory response in all considered brain regions. In contrast, CNMs were well-tolerated in the brain parenchyma, with assessments at both molecular and histological levels revealing only an acute response at days 1 and 2 followed by fast recovery by day 7. No significant differences were observed between the two types of MWNT functionalisation or the two doses of CNMs (1 µg *vs* 0.5 µg). Among the different CNMs, GO nanosheets displayed the least deleterious profile, with even some beneficial immunomodulatory properties that mitigate the inherent inflammation and brain tissue damages associated with the brain stereotactic administration. Therefore, under the conditions tested here, GO nanosheets appeared to have the best profile for future development as brain nanovector, especially for cerebral applications that require focal drug administration or in conditions with an inherent inflammatory component. Going further, additional investigations should examine not only the long-term fate and chronic effects of these materials after their injection in the brain, but also the long-term consequences of the apparent immunomodulation properties of GO.

Experimental Section

Nanomaterials production

Functionalised multi-walled carbon nanotubes. Pristine MWNTs were purchased from Nanostructured and Amorphous Materials Inc. (NanoAmorph, Houston, TX, USA) with a carbon content of 94%. The pristine materials were then modified using either a 1,3-dipolar cycloaddition reaction to obtain aminated MWNTs (MWNT-NH_3^+) or a 24-h reaction in H_2SO_4/HNO_3 (3:1) solution to produce carboxylated MWNTs (ox-MWNT), as previously described [72, 73].

Graphene oxide sheets. GO flake suspensions in water were prepared from graphite powder (Merck, Sigma-Aldrich, UK) and synthesis was conducted using a modified Hummers' method as previously described [56, 57].

Liposomes. To produce liposomes, 1,2-dioleoyl-3-trimethylammonium-propane hydrochloride (DOTAP) and 1,2-dioleoyl-sn-glycero-3-[phospho-rac-(3-lysyl(1-glycerol))] (DOPG) were kindly provided by Lipoid GmbH (Ludwigshafen, Germany). Cholesterol (CHOL) was purchased from Merck Sigma-Aldrich (UK). Chloroform and methanol were purchased from Thermo Fisher Scientific (UK). Both cationic (DOTAP/CHOL; 2 mM DOTAP:1 mM CHOL) and anionic (DOPG/CHOL; 2 mM DOPG:1 mM CHOL) liposomes were prepared using the film hydration method [74]. Briefly, DOTAP or DOPG and CHOL were dissolved in chloroform/methanol (4:1, v/v) and the organic solvents were evaporated under pressure for 30 min at +40°C using a rotary evaporator. The resulting thin lipid film was hydrated in sterile-filtered 5% (w/v) dextrose solution in water and then bath sonicated for 15 min at +40°C. The final liposome solution was kept at room temperature for 30 min to stabilize the colloidal stability before storage at +4°C for a maximum of 5 days.

Characterization of the nanomaterials

Functionalised multi-walled carbon nanotubes. MWNTs were analysed by transmission electron microscopy (TEM) to determine the mean diameter and length as previously described for the aminated and carboxylated MWNTs [37, 73]. A Kaiser test was used for MWNT-NH_3^+ to measure the amount of amine functionalization as previously reported [72]. Kaiser test is based on the colorimetric reaction between the ninhydrin reagent and the amine groups. The reaction gives a blue colour readout and the intensity in proportionally related to the amount of free terminal amine groups [75]. DLS was not used to assess hydrodynamic diameter of the GO sheets, as it has been proven non reliable for one dimensional tube-shaped or two-dimensional plate-shaped materials. More systemic characterisation of these materials has been previously reported.

Graphene oxide sheets. GO sheets were characterised by several techniques, including dynamic light scattering (DLS, Nano Zeta Sizer ZS, ZEN3600, Malvern Panalytical, Malvern, UK), TEM (Philips/FEI, Thermo Fisher Scientific, UK), and atomic force microscopy (AFM, Bruker, UK) to assess physicochemical properties. These properties include ζ-potential, lateral dimensions, and the thickness of the sheets. DLS was not used to assess hydrodynamic diameter of the GO sheets, as it has been proven non reliable for two-dimensional plate-shaped or one dimensional tube-shaped materials. More systemic characterisation of these materials were reported previously [57] (in this reference, the GO sheets used herein are named small GO).

Liposomes. Liposomes were first characterised by the DLS technique. Particle diameter and electrophoretic mobility of cationic and anionic liposomes were measured at 25 ± 0.1°C using a Zeta-Sizer unit (Nano Zeta Sizer ZS, ZEN3600, Malvern Panalytical, Malvern, UK). The particle size is based on DLS in back-scattering mode, at 173° and excitation λ=632.8 nm. For electrophoretic

mobility measurements, dispersions were placed into U-shaped cuvettes equipped with gold electrodes. The ζ-potential is related to the electrophoretic mobility by Henry's equation valid in the Smoluchowski approximation, when the screening length is much smaller than the particle radius. The prepared liposomes were also analysed using TEM (Philips/FEI, Thermo Fisher Scientific, UK).

Preparation of nanomaterials for brain injection

Functionalised multi-walled carbon nanotubes. The day before injection, dry powders of MWNT-NH_3^+ and ox-MWNT were weighed, exposed to low energy UV light for 6 hours in order to "sterilise" the nanotubes, and then rehydrated with sterile-filtered 5% dextrose solution in water (final concentration 1 mg/mL) in sterilised glass container. This material suspension was initially sonicated for 45 min using a water bath sonicator (VWR, UK) operating at 80 W (45 kHz) to allow dispersion of the nanotubes in the dextrose solution. A 0.5 mg/mL suspension was achieved by further dilution in sterile-filtered 5% dextrose solution. All colloidal suspensions kept at +4°C were sonicated for an additional 15 min immediately before the injection.

Graphene oxide sheets. Dry powder of GO sheets that were exposed to UV light for 6 hours after weighting was also rehydrated in sterile-filtered 5% dextrose solution at a concentration of 1 mg/mL. This suspension was sonicated for 30 min using a water bath sonicator (VWR, UK) operating at 80 W (45 kHz) to allow dispersion of GO flakes in the dextrose solution. The 0.5 mg/mL suspension used here was achieved by further dilution in sterile-filtered 5% dextrose solution.

Liposomes. Liposomes were initially prepared at 2 mM DOTAP:1 mM Chol or 2 mM DOPG:1 mM Chol and then further diluted to the final concentration of 1 mg/mL in sterile-filtered 5% dextrose solution.

The vehicle used for all nanomaterials, sterile-filtered 5% dextrose solution, was used as negative control (*i.e.* basic conditions of inflammation following stereotactic injection of an isotonic solution, such as 5% dextrose in water). Lipopolysaccharide (LPS) O111:B4 suspension at 5 mg/mL in sterile-filtered 5% dextrose solution was used as positive control for inflammatory reaction [37].

Animals and sample preparation

A total of 84 young (3-week-old) C57BL/6 male mice were used. The protocol received ethical approval from the University of Manchester under authorisation from the United Kingdom Home Office (project License number PPL-70/7763). Suffering was minimised and the minimal number of animals were used in accordance with the Code of Practice for the housing and care of animals used in scientific procedures. The animals were kept in groups of four to five in standard cages with free access to food and water under controlled environmental conditions, including a 12 h/12 h light/dark cycle.

For surgery, mice were initially anesthetised with isoflurane inhalation, injected with analgesic (Buprenorphine 0.1 mg/kg, *im*), and then placed on a stereotactic apparatus. A hole was drilled in the skull at specific lateral coordinates. A total of 1 µl of the different nanomaterials suspended in 5% dextrose in water was injected in the striatum with a micro-syringe mounted on a stereotaxic holder (coordinates used: lateral (*x*) -0.1 mm, ventral (*y*) -2.3 mm, rostro-caudal (*z*) -3.0 mm from bregma) [76].

During the surgical procedure, the mice were kept under oxygen and heated using a blanket with a thermostat to maintain body temperature at approximately 37°C. At the end of the procedure, the wound was sutured and the animal was maintained in a thermally controlled incubation chamber at 37°C until complete recovery from anaesthesia. The mice were then returned to their maintenance cages and culled at different time points as shown in the experimental design (**Figure 1-A**).

Mice used for gene expression analyses were sacrificed at 1 day, 2 days, or 7 days after injection (*n* = 3 per group; total of 63 mice). They were culled with CO_2 exposure followed by cerebral dislocation. The brain was then rapidly dissected out and cut into 2 mm thick slices using a Zivic stainless brain slicer matrix. For each brain, four coronal slices were prepared: one containing the injected area, one immediately posterior to assess diffusion of nanomaterials or of signal in a region adjacent to the injection, and two anterior to the injected area. The most anterior of the latter two slices was used to assess diffusion of nanomaterials or of signal in a distant brain region. From the three brain slices thus sampled, a 2 x 2 x 2 mm tissue block was dissected for RT-qPCR analysis (**Figure 1-A**). In the slice containing the injection site, the sampled tissue block was centred on this site. In the adjacent posterior slice and in the anterior slice, the tissue blocks were sampled along the same antero-posterior and dorso-ventral axes of the injection site. The tissue blocks were snap-frozen in liquid nitrogen and cryopreserved for RNA extraction and real-time RT-qPCR analysis.

Animals for colorimetric histochemical and immuno-histochemical procedures were sacrificed at day 2 after injection (*n* = 3 per group; total of 21 mice). They were anaesthetised by isoflurane inhalation and then cardiac-perfused with 4% paraformaldehyde in 0.01 M phosphate-buffered saline, pH 7.4 (PBS). The brain was then dissected out and immersed overnight in 4% paraformaldehyde in PBS. The following day, brains were soaked in sucrose (5%, 15%, 30% steps) at 4°C for cryoprotection following a previously described procedure [37].

Real-Time Quantitative PCR analysis

Tissue blocks from animals injected with GO (0.5 mg/mL), MWNT-NH_3^+ (0.5 mg/mL), ox-MWNT (0.5 mg/mL), cationic liposomes (1 mg/mL), anionic liposomes (1 mg/mL), 5% dextrose (vehicle, negative control), or LPS (positive control) were used for transcript analysis. Tissue blocks were homogenised with a TissueLyser LT (Qiagen, Netherlands) and total RNA was extracted using a NucleoSpin RNA/Protein kit (Macherey-Nagel, Germany) according to the manufacturer's instructions. The concentration of RNA was determined as the optical density ratio 260 nm/280 nm using a

BioPhotometer plus (Eppendorf, Germany). Ratio values between 1.8 and 2.2 were considered good quality. Samples of cDNA were prepared from 1 mg RNA in a total volume of 20 µl using the BioRad iScript cDNA Synthesis Kit (BioRad, USA). Samples were run on a CFX-96 Real Time Detection System (BioRad, USA) with the following sequence: 95°C for 3 min (initial denaturation step), 1 cycle; 95°C for 10 sec (amplification), 60°C for 30 sec (annealing), repeated for 40 cycles. Amplification was followed by a melting-curve analysis to confirm PCR product specificity.

Each RT-PCR reaction in a 25 µl total volume contained 2 µl of cDNA from reverse transcription PCR, 12.5 µl Fast SYBR Green Master Mix (BioRad, UK), and primers at 200 nM each (Merck-Sigma-Aldrich, UK; see **Table S1** for reverse and forward primer sequences). Gene expression levels (*tnf-α*, *il-1β*, *il-6*, *il-12*, *ifn-γ*, *cxcl10*, *ccl2, il-10*, *tgf-β*, *il-4*, and housekeeping gene *β-actin*) were calculated using the Livak method, based on calculation of $2^{-\Delta\Delta CT}$ [77]. *β-actin* was used as a reference housekeeping gene to normalise the amount of target primer transcripts. The normalised values for each gene were compared to the relative expression for 5% dextrose (negative control) to calculate the fold increase of the target gene in the sample.

Immuno-histochemical and histochemical procedures

Tissue processing. Brains (day 2 post injection) from animals injected with GO (0.5 and 1 mg/mL), MWNT-NH_3^+ (0.5 and 1 mg/mL), ox-MWNT (0.5 and 1 mg/mL), cationic liposomes (1 mg/mL), anionic liposomes (1 mg/mL), 5% dextrose (vehicle, negative control), or LPS (positive control) were used for cell analyses.

Following cardiac perfusion of fixative under anaesthesia (as described above), post-fixation, and brain cryoprotection in sucrose, brains were snap-frozen and then cut using a cryo-microtome into 30-µm-thick serial coronal sections. Series of sections (one every 360 µm) were collected in the following three regions*: i)* anterior to the injection site (from +1.9 to +1.0 from bregma), *ii)* at the injection site (from -0.1 to -0.9 from bregma), and *iii)* posterior to it (from -1.2 to -2.0 from bregma).

Immuno-phenotyping of neurons, microglia, astrocytes, and apoptotic cells. For each experimental group (*n = 3* animals per group), a series of sections was processed for immuno-histochemistry. Free-floating sections were pre-treated with 1% H_2O_2 (Merck Sigma-Aldrich, UK) for 15 sec at room temperature, rinsed in PBS (Merck Sigma-Aldrich, UK), and incubated in 5% Normal Serum of the appropriate species (Vector Lab, USA; **Table S2**), and 0.03% Triton-X100 (Merck Sigma-Aldrich, UK) in PBS for 1 h at room temperature to prevent nonspecific binding. After rinsing in PBS, the sections were incubated overnight at 4°C in primary antibodies (**Table S2**) diluted in 1% Normal Serum in PBS. The sections were then incubated in biotinylated secondary antibodies (Vector Lab) in 1% Normal Serum in PBS. The sections were then reacted with the Vectastain ABC kit (Vector Lab) and finally with 0.5% 3-3’ diaminobenzidine (DAB, Merck-Sigma-Aldrich) in PBS. After rinsing, the sections were dehydrated through an increasing alcohol gradient, mounted, and

cover-slipped. The sections were examined with an Olympus microscope equipped with a QICAM digital camera (QImaging, Canada) using Image-Pro Plus 7.0 Software (Media Cybernetics, USA).

Fluoro-Jade B histochemistry. To evaluate ongoing neuronal cell death, Fluoro-Jade B staining was performed [60]. Sections were mounted on gelatin-coated slides, air dried, and soaked for 5 min in 1% NaOH (Merck-Sigma-Aldrich) in 80% alcohol in distilled water. The sections were then soaked for 2 min in 70% alcohol and 2 min in distilled water, and then in a solution of 0.06% potassium permanganate (Merck Sigma-Aldrich) for 10 min to reduce the background signal. The sections were then rinsed in distilled water for 2 min and soaked for 15 min in the staining solution. The Fluoro-Jade B working solution (0.0004%) was obtained by diluting 4 mL of 0.01% stock solution (10 mg of powder [Histochem Inc., USA] in 100 mL of distilled water) into 96 mL of 0.1% acetic acid (Merck Sigma-Aldrich). The sections were then rinsed in distilled water and air dried. They were cleared in xylene for 2 min, mounted, and then cover-slipped. The sections were analysed with an Olympus microscope equipped with a UV bulb light source (450-490 nm blue excitation light filter; Fluoro-Jade B has a green light emission) and images were taken with a QICAM digital camera (QImaging, Surrey, BC, Canada).

Quantitative analyses

Counts of neurons and astrocytes. To assess whether the intra-striatal injection of nanomaterials induced neuronal cell loss, the number of neurons identified by NeuN immunoreactivity was estimated using a stereological approach in all groups of mice (animals sacrificed at day 2 after injection of all the materials; *n* = 3 per group; total of 21 mice).

Stereology was also used to estimate the number of astrocytes. This was based on glial fibrillary acidic protein (GFAP) immunostaining in the mice treated with 5% dextrose, LPS, or cationic liposomes. Cell counting was performed using three regions of interest (ROIs) per section in six sections (2 regularly spaced sections through the anterior region, the injection site, and the posterior region, respectively) per mouse and three mice per group. The counting of astrocytes was performed in three ROIs per section in six sections sampled as above per mouse and three mice per group. Sections were analysed with an Olympus microscope equipped with a Retiga-2000R CCD Camera (QImaging, Canada) and counting was performed with the Optical Fractionator probe included in Stereo Investigator 10 software (MBF Bioscience, USA).

Analysis of glial cell coverage and optical density of microglial cells. A series of sections for each condition (*n = 3*; immunostained as described above for visualisation of microglial cells and astrocytes) were used to assess the percentage of the area covered by CD11b- and GFAP-immuno-positive cells, assuming that a larger area is covered by activated glial cells than by “resting” cells [78, 79]. The immunostaining was thus quantified as the percentage of the total image area, considering the site of injection in the striatum and an equivalent ROI in the anterior and posterior sections.

The intensity of the CD11b immunoreactivity was also quantified by densitometry. A quantitative densitometric analysis [80-82] was performed to measure (in the same sections) the intensity of immunoreactivity signal in the cell somata [83]. For this analysis, three ROIs (with an area of 289 μm^2) per section in six sections per mouse sampled as above and in three mice per group were used. Sections were analysed with an Olympus microscope and 8-bit grey-scale images were taken with a 20X objective and a QImaging QICAM digital camera (QImaging, Canada) maintaining constant light conditions and magnification. Images were then processed using the Image-Pro Plus 7.0 software (Media Cybernetics, USA). A signal from non-immunostained tissue (contralateral hemisphere) was used to subtract the background signal.

Statistics

The results were expressed as mean per group ± standard error of the mean (SEM). The Livak method was used to analyse qPCR data using ΔCT values [77]. Data were checked for normal distribution before running statistical analysis. Statistical variations were evaluated as follows: for simple comparisons unpaired t-tests were used and one-way analysis of variance (ANOVA) per group, followed by Bonferroni *post-hoc* for testing pairwise comparisons. For immuno-histochemical and histochemical analysis, the number of sample units used in each study group (n=3) has been compensated by different measures of the parameter (3 different ROIs) in the areas of interest, within the brain (anterior site, injection site, and posterior site). GraphPad Prism (GraphPad Software v.6) was used for statistical analyses. p-values < 0.05 were considered significant.

Supporting Information

Supporting Information is available from the Wiley Online Library or from the author.
Pdf document attached.

Funding

This work was partly supported by the EU H2020 RTD Framework Program: FET Graphene Flagship project (H2020-EU.1.2.3.- FET Flagships; GrapheneCore; 2785219), the Centre National de la Recherche Scientifique (CNRS), the International Center for Frontier Research in Chemistry (icFRC), and the Agence Nationale de la Recherche (ANR) through the LabEx project Chemistry of Complex Systems (ANR-10-LABX-0026_CSC). Financial support to this project was partially provided by The Fondazione Cariverona ("*Verona Nanomedicine Initiative*") and funding from an intramural (University of Verona) international cooperation program ("*CooperInt*") was obtained. KK would like to acknowledge the Severo Ochoa Centre of Excellence Award to ICN2.

Authors' contributions

CP, CB, and KK conceived the overall design of the project. CP and CB implemented the experiments and analysed the data under the supervision of CB, KK, and MB, with contributions from MM, DAJ, and NL. DAJ prepared the GO sheets and NL prepared the liposomes. AB and MP provided the carbon nanotubes. CP and CB wrote the manuscript draft. All authors contributed to manuscript editing and approved its content.

Acknowledgments

The authors would like to thank Dr Irene de Lázaro for fruitful discussion regarding statistical analyses of the RT-qPCR data, Ms Lana Papafilippou for the TEM imaging of the cationic liposomes, and Dr Marco Sandri (Big and Open Data Innovation Laboratory - BODaI-Lab, University of Brescia, Italy) for the valuable scientific support in the biostatistical analysis of the data. Graphical abstract and Figure 1A were created using BioRender.com.

Data Availability

The raw/processed data required to reproduce these findings cannot be shared at this time as the data also forms part of an ongoing study.

References

[1] D. Furtado, M. Bjornmalm, S. Ayton, A.I. Bush, K. Kempe, F. Caruso, 2018. Overcoming the blood-brain barrier: The role of nanomaterials in treating neurological diseases. Adv Mater. 30, e1801362. https://doi.org/10.1002/adma.201801362.

[2] Y. Cheng, R.A. Morshed, B. Auffinger, A.L. Tobias, M.S. Lesniak, Multifunctional nanoparticles for brain tumor imaging and therapy, Adv Drug Deliv Rev. 66 (2014) 42-57. https://doi.org/10.1016/j.addr.2013.09.006

[3] L. Biddlestone-Thorpe, N. Marchi, K. Guo, C. Ghosh, D. Janigro, K. Valerie, H. Yang, Nanomaterial-mediated cns delivery of diagnostic and therapeutic agents, Adv Drug Deliv Rev. 64 (2012) 605-613. https://doi.org/10.1016/j.addr.2011.11.014.

[4] A. Dominguez, B. Suarez-Merino, F. Goni-de-Cerio, Nanoparticles and blood-brain barrier: The key to central nervous system diseases, J Nanosci Nanotechnol. 14 (2014) 766-779. https://doi.org/10.1166/jnn.2014.9119.

[5] G. Modi, V. Pillay, Y.E. Choonara, V.M. Ndesendo, L.C. du Toit, D. Naidoo, Nanotechnological applications for the treatment of neurodegenerative disorders, Prog Neurobiol. 88 (2009) 272-285. https://doi.org/10.1016/j.pneurobio.2009.05.002.

[6] M. Caffo, L. Merlo, D. Marino, G. Caruso, Graphene in neurosurgery: The beginning of a new era, Nanomedicine (Lond). 10 (2015) 615-625. https://doi.org/10.2217/nnm.14.195.

[7] J.T. Wang, K.T. Al-Jamal, Functionalized carbon nanotubes: Revolution in brain delivery, Nanomedicine (Lond). 10 (2015) 2639-2642. 10.2217/nnm.15.114.

[8] H. Kafa, J.T. Wang, K.T. Al-Jamal, Current perspective of carbon nanotubes application in neurology, Int Rev Neurobiol. 130 (2016) 229-263. https://doi.org/10.1016/bs.irn.2016.07.001.

[9] B.S. Wong, S.L. Yoong, A. Jagusiak, T. Panczyk, H.K. Ho, W.H. Ang, G. Pastorin, Carbon nanotubes for delivery of small molecule drugs, Adv Drug Deliv Rev. 65 (2013) 1964-2015. https://doi.org/10.1016/j.addr.2013.08.005.

[10] M. Bramini, G. Alberini, E. Colombo, M. Chiacchiaretta, M.L. DiFrancesco, J.F. Maya-Vetencourt, L. Maragliano, F. Benfenati, F. Cesca, Interfacing graphene-based materials with neural cells, Front Syst Neurosci. 12 (2018) 12. https://doi.org/10.3389/fnsys.2018.00012.

[11] A. Bianco, K. Kostarelos, C.D. Partidos, M. Prato, Biomedical applications of functionalised carbon nanotubes, Chem Commun (Camb). 5 (2005) 571-577. https://doi.org/10.1039/b410943k.
[12] A. Bianco, K. Kostarelos, M. Prato, Applications of carbon nanotubes in drug delivery, Curr Opin Chem Biol. 9 (2005) 674-679. https://doi.org/10.1016/j.cbpa.2005.10.005.
[13] L. Lacerda, A. Bianco, M. Prato, K. Kostarelos, Carbon nanotubes as nanomedicines: From toxicology to pharmacology, Adv Drug Deliv Rev. 58 (2006) 1460-1470. https://doi.org/10.1016/j.addr.2006.09.015.
[14] K. Kostarelos, K.S. Novoselov, Graphene devices for life, Nat Nanotechnol. 9 (2014) 744-745. https://doi.org/10.1038/nnano.2014.224.
[15] T.A. Mattei, How graphene is expected to impact neurotherapeutics in the near future, Expert Rev Neurother. 14 (2014) 845-847. https://doi.org/10.1586/14737175.2014.925804.
[16] X. Guo, N. Mei, Assessment of the toxic potential of graphene family nanomaterials, J Food Drug Anal. 22 (2014) 105-115. https://doi.org/10.1016/j.jfda.2014.01.009.
[17] K. Zhou, G.A. Thouas, C.C. Bernard, D.R. Nisbet, D.I. Finkelstein, D. Li, J.S. Forsythe, Method to impart electro- and biofunctionality to neural scaffolds using graphene–polyelectrolyte multilayers, ACS Appl Mater Interfaces. 4 (2012) 4524-4531. https://doi.org/10.1021/am3007565.
[18] S.M. Chowdhury, C. Surhland, Z. Sanchez, P. Chaudhary, M.A. Suresh Kumar, S. Lee, L.A. Pena, M. Waring, B. Sitharaman, M. Naidu, Graphene nanoribbons as a drug delivery agent for lucanthone mediated therapy of glioblastoma multiforme, Nanomedicine. 11 (2015) 109-118. https://doi.org/10.1016/j.nano.2014.08.001.
[19] J. Ren, S. Shen, D. Wang, Z. Xi, L. Guo, Z. Pang, Y. Qian, X. Sun, X. Jiang, The targeted delivery of anticancer drugs to brain glioma by pegylated oxidized multi-walled carbon nanotubes modified with angiopep-2, Biomaterials. 33 (2012) 3324-3333. https://doi.org/10.1016/j.biomaterials.2012.01.025.
[20] M.K. Gottipati, E. Bekyarova, R.C. Haddon, V. Parpura, Chemically functionalized single-walled carbon nanotubes enhance the glutamate uptake characteristics of mouse cortical astrocytes, Amino Acids. 47 (2015) 1379-1388. https://doi.org/10.1007/s00726-015-1970-9.
[21] X. Xue, L.R. Wang, Y. Sato, Y. Jiang, M. Berg, D.S. Yang, R.A. Nixon, X.J. Liang, Single-walled carbon nanotubes alleviate autophagic/lysosomal defects in primary glia from a mouse model of alzheimer's disease, Nano Lett. 14 (2014) 5110-5117. https://doi.org/10.1021/nl501839q.
[22] K.T. Al-Jamal, L. Gherardini, G. Bardi, A. Nunes, C. Guo, C. Bussy, M.A. Herrero, A. Bianco, M. Prato, K. Kostarelos, T. Pizzorusso, Functional motor recovery from brain ischemic insult by carbon nanotube-mediated sirna silencing, Proc Natl Acad Sci USA. 108 (2011) 10952-10957. https://doi.org/10.1073/pnas.1100930108.
[23] Z. Yang, Y. Zhang, Y. Yang, L. Sun, D. Han, H. Li, C. Wang, Pharmacological and toxicological target organelles and safe use of single-walled carbon nanotubes as drug carriers in treating alzheimer disease, Nanomedicine. 6 (2010) 427-441. https://doi.org/10.1016/j.nano.2009.11.007.
[24] H. Kafa, J.T. Wang, N. Rubio, K. Venner, G. Anderson, E. Pach, B. Ballesteros, J.E. Preston, N.J. Abbott, K.T. Al-Jamal, The interaction of carbon nanotubes with an in vitro blood-brain barrier model and mouse brain in vivo, Biomaterials. 53 (2015) 437-452. https://doi.org/10.1016/j.biomaterials.2015.02.083.
[25] S. Shityakov, E. Salvador, G. Pastorin, C. Forster, Blood-brain barrier transport studies, aggregation, and molecular dynamics simulation of multiwalled carbon nanotube functionalized with fluorescein isothiocyanate, Int J Nanomedicine. 10 (2015) 1703-1713. https://doi.org/10.2147/IJN.S68429.
[26] H. Kafa, J.T. Wang, N. Rubio, R. Klippstein, P.M. Costa, H.A. Hassan, J.K. Sosabowski, S.S. Bansal, J.E. Preston, N.J. Abbott, K.T. Al-Jamal, Translocation of lrp1 targeted carbon nanotubes of different diameters across the blood-brain barrier in vitro and in vivo, J Control Release. 225 (2016) 217-229. https://doi.org/10.1016/j.jconrel.2016.01.031.
[27] J.T. Wang, N. Rubio, H. Kafa, E. Venturelli, C. Fabbro, C. Menard-Moyon, T. Da Ros, J.K. Sosabowski, A.D. Lawson, M.K. Robinson, M. Prato, A. Bianco, F. Festy, J.E. Preston, K. Kostarelos, K.T. Al-Jamal, Kinetics of functionalised carbon nanotube distribution in mouse brain after systemic injection: Spatial to ultra-structural analyses, J Control Release. 224 (2016) 22-32. https://doi.org/10.1016/j.jconrel.2015.12.039.
[28] Y. Liu, L.P. Xu, W. Dai, H. Dong, Y. Wen, X. Zhang, Graphene quantum dots for the inhibition of beta amyloid aggregation, Nanoscale. 7 (2015) 19060-19065. https://doi.org/10.1039/c5nr06282a.
[29] M. Li, X. Yang, J. Ren, K. Qu, X. Qu, Using graphene oxide high near-infrared absorbance for photothermal treatment of alzheimer's disease, Adv Mater. 24 (2012) 1722-1728. 10.1002/adma.201104864.

[30] L. Feng, L. Wu, X. Qu, New horizons for diagnostics and therapeutic applications of graphene and graphene oxide, Adv Mater. 25 (2013) 168-186. 10.1002/adma.201203229.
[31] G. Liu, H. Shen, J. Mao, L. Zhang, Z. Jiang, T. Sun, Q. Lan, Z. Zhang, Transferrin modified graphene oxide for glioma-targeted drug delivery: In vitro and in vivo evaluations, ACS Appl Mater Interfaces. 5 (2013) 6909-6914. https://doi.org/10.1021/am402128s.
[32] Y. Kang, J. Liu, S. Yin, Y. Jiang, X. Feng, J. Wu, Y. Zhang, A. Chen, Y. Zhang, L. Shao, Oxidation of reduced graphene oxide via cellular redox signaling modulates actin-mediated neurotransmission, ACS NANO. (2020). 10.1021/acsnano.9b08078.
[33] H. Peluffo, U. Unzueta, M.L. Negro-Demontel, Z. Xu, E. Vaquez, N. Ferrer-Miralles, A. Villaverde, Bbb-targeting, protein-based nanomedicines for drug and nucleic acid delivery to the cns, Biotechnol Adv. 33 (2015) 277-287. https://doi.org/10.1016/j.biotechadv.2015.02.004
[34] M.W. Salter, B. Stevens, Microglia emerge as central players in brain disease, Nat Med. 23 (2017) 1018-1027. https://doi.org/10.1038/nm.4397.
[35] M. Bentivoglio, R. Mariotti, G. Bertini, Neuroinflammation and brain infections: Historical context and current perspectives, Brain Res Rev. 66 (2011) 152-173. https://doi.org/10.1016/j.brainresrev.2010.09.008.
[36] G. Bardi, P. Tognini, G. Ciofani, V. Raffa, M. Costa, T. Pizzorusso, Pluronic-coated carbon nanotubes do not induce degeneration of cortical neurons in vivo and in vitro, Nanomedicine. 5 (2009) 96-104. https://doi.org/10.1016/j.nano.2008.06.008.
[37] G. Bardi, A. Nunes, L. Gherardini, K. Bates, K.T. Al-Jamal, C. Gaillard, M. Prato, A. Bianco, T. Pizzorusso, K. Kostarelos, 2013. Functionalized carbon nanotubes in the brain: Cellular internalization and neuroinflammatory responses. PLoS One. 8, e80964. https://doi.org/10.1371/journal.pone.0080964.
[38] L. Dal Bosco, G.E. Weber, G.M. Parfitt, K. Paese, C.O. Goncalves, T.M. Serodre, C.A. Furtado, A.P. Santos, J.M. Monserrat, D.M. Barros, Pegylated carbon nanotubes impair retrieval of contextual fear memory and alter oxidative stress parameters in the rat hippocampus, Biomed Res Int. 2015 (2015) 1-11. https://doi.org/10.1155/2015/104135.
[39] L. Dal Bosco, G.E. Weber, G.M. Parfitt, A.P. Cordeiro, S.K. Sahoo, C. Fantini, M.C. Klosterhoff, L.A. Romano, C.A. Furtado, A.P. Santos, J.M. Monserrat, D.M. Barros, 2015. Biopersistence of pegylated carbon nanotubes promotes a delayed antioxidant response after infusion into the rat hippocampus. PLoS One. 10, e0129156. https://doi.org/10.1371/journal.pone.0129156.
[40] C. Bussy, K.T. Al-Jamal, J. Boczkowski, S. Lanone, M. Prato, A. Bianco, K. Kostarelos, Microglia determine brain region-specific neurotoxic responses to chemically functionalized carbon nanotubes, ACS NANO. 9 (2015) 7815-7830. https://doi.org/10.1021/acsnano.5b02358.
[41] L. Yang, F. Wang, H. Han, L. Yang, G. Zhang, Z. Fan, Functionalized graphene oxide as a drug carrier for loading pirfenidone in treatment of subarachnoid hemorrhage, Colloids Surf B Biointerfaces. 129 (2015) 21-29. https://doi.org/10.1016/j.colsurfb.2015.03.022.
[42] R. Rauti, N. Lozano, V. Leon, D. Scaini, M. Musto, I. Rago, F.P. Ulloa Severino, A. Fabbro, L. Casalis, E. Vazquez, K. Kostarelos, M. Prato, L. Ballerini, Graphene oxide nanosheets reshape synaptic function in cultured brain networks, ACS NANO. 10 (2016) 4459-4471. https://doi.org/10.1021/acsnano.6b00130.
[43] M. Bramini, S. Sacchetti, A. Armirotti, A. Rocchi, E. Vazquez, V. Leon Castellanos, T. Bandiera, F. Cesca, F. Benfenati, Graphene oxide nanosheets disrupt lipid composition, ca(2+) homeostasis, and synaptic transmission in primary cortical neurons, ACS NANO. 10 (2016) 7154-7171. https://doi.org/10.1021/acsnano.6b03438.
[44] M. Chiacchiaretta, M. Bramini, A. Rocchi, A. Armirotti, E. Giordano, E. Vazquez, T. Bandiera, S. Ferroni, F. Cesca, F. Benfenati, Graphene oxide upregulates the homeostatic functions of primary astrocytes and modulates astrocyte-to-neuron communication, Nano Lett. (2018). https://doi.org/10.1021/acs.nanolett.8b02487.
[45] C. Hoyle, J. Rivers-Auty, E. Lemarchand, S. Vranic, E. Wang, M. Buggio, N.J. Rothwell, S.M. Allan, K. Kostarelos, D. Brough, Small, thin graphene oxide is anti-inflammatory activating nuclear factor erythroid 2-related factor 2 via metabolic reprogramming, ACS NANO. 12 (2018) 11949-11962. https://doi.org/10.1021/acsnano.8b03642.
[46] H. Lv, S. Zhang, B. Wang, S. Cui, J. Yan, Toxicity of cationic lipids and cationic polymers in gene delivery, J Control Release. 114 (2006) 100-109. https://doi.org/10.1016/j.jconrel.2006.04.014.
[47] M.C. Filion, N.C. Phillips, Toxicity and immunomodulatory activity of liposomal vectors formulated with cationic lipids toward immune effector cells, Biochim Biophys Acta. 1329 (1997) 345-356. https://doi.org/10.1016/S0005-2736(97)00126-0.
[48] K.B. Knudsen, H. Northeved, P.K. Ek, A. Permin, T.L. Andresen, S. Larsen, K.M. Wegener, H.R. Lam, J. Lykkesfeldt, Differential toxicological response to positively and negatively charged

nanoparticles in the rat brain, Nanotoxicology. 8 (2014) 764-774.
https://doi.org/10.3109/17435390.2013.829589.
[49] K.B. Knudsen, H. Northeved, P.E. Kumar, A. Permin, T. Gjetting, T.L. Andresen, S. Larsen, K.M. Wegener, J. Lykkesfeldt, K. Jantzen, S. Loft, P. Moller, M. Roursgaard, In vivo toxicity of cationic micelles and liposomes, Nanomedicine. 11 (2015) 467-477.
https://doi.org/10.1016/j.nano.2014.08.004.
[50] R. Rauti, M. Medelin, L. Newman, S. Vranic, G. Reina, A. Bianco, M. Prato, K. Kostarelos, L. Ballerini, Graphene oxide flakes tune excitatory neurotransmission in vivo by targeting hippocampal synapses, Nano Lett. 19 (2019) 2858-2870. 10.1021/acs.nanolett.8b04903.
[51] C. Klumpp, K. Kostarelos, M. Prato, A. Bianco, Functionalized carbon nanotubes as emerging nanovectors for the delivery of therapeutics, Biochim Biophys Acta. 1758 (2006) 404-412.
10.1016/j.bbamem.2005.10.008.
[52] A. Bianco, K. Kostarelos, M. Prato, Making carbon nanotubes biocompatible and biodegradable, Chem Commun 47 (2011) 10182-10188. 10.1039/c1cc13011k.
[53] A. Nunes, C. Bussy, L. Gherardini, M. Meneghetti, M.A. Herrero, A. Bianco, M. Prato, T. Pizzorusso, K.T. Al-Jamal, K. Kostarelos, *In vivo* degradation of functionalized carbon nanotubes after stereotactic administration in the brain cortex, Nanomedicine (Lond). 7 (2012) 1485-1494.
https://doi.org/10.2217/nnm.12.33.
[54] A. Nunes, K. Al-Jamal, T. Nakajima, M. Hariz, K. Kostarelos, Application of carbon nanotubes in neurology: Clinical perspectives and toxicological risks, Arch Toxicol. 86 (2012) 1009-1020.
https://doi.org/10.1007/s00204-012-0860-0.
[55] C. Bussy, C. Hadad, M. Prato, A. Bianco, K. Kostarelos, Intracellular degradation of chemically functionalized carbon nanotubes using a long-term primary microglial culture model, Nanoscale. 8 (2016) 590-601. 10.1039/c5nr06625e.
[56] A.D. Jasim, N. Lozano, K. Kostarelos, 2016. Synthesis of few-layered, high-purity graphene oxide sheets from different graphite sources for biology. 2D materials. 3, 014006.
https://doi.org/10.1088/2053-1583/3/1/014006.
[57] A.F. Rodrigues, L. Newman, N. Lozano, S.P. Mukherjee, B. Fadeel, C. Bussy, K. Kostarelos, 2018. A blueprint for the synthesis and characterisation of thin graphene oxide with controlled lateral dimensions for biomedicine. 2D materials. 5, 035020. https://doi.org/10.1088/2053-1583/aac05c.
[58] C. Mamot, J.B. Nguyen, M. Pourdehnad, P. Hadaczek, R. Saito, J.R. Bringas, D.C. Drummond, K. Hong, D.B. Kirpotin, T. McKnight, M.S. Berger, J.W. Park, K.S. Bankiewicz, Extensive distribution of liposomes in rodent brains and brain tumors following convection-enhanced delivery, J Neurooncol. 68 (2004) 1-9. https://doi.org/10.1023/B:NEON.0000024743.56415.4b.
[59] L. Gallentoft, L.M. Pettersson, N. Danielsen, J. Schouenborg, C.N. Prinz, C.E. Linsmeier, Size-dependent long-term tissue response to biostable nanowires in the brain, Biomaterials. 42 (2015) 172-183. https://doi.org/10.1016/j.biomaterials.2014.11.051.
[60] L.C. Schmued, K.J. Hopkins, Fluoro-jade b: A high affinity fluorescent marker for the localization of neuronal degeneration, Brain Res. 874 (2000) 123-130. https://doi.org/10.1016/S0006-8993(00)02513-0.
[61] V. Mirshafiee, W. Jiang, B. Sun, X. Wang, T. Xia, Facilitating translational nanomedicine via predictive safety assessment, Mol Ther. 25 (2017) 1522-1530.
https://doi.org/10.1016/j.ymthe.2017.03.011.
[62] P. Møller, J. Lykkesfeldt, Positive charge, negative effect: The impact of cationic nanoparticles in the brain, Nanomedicine (Lond). 9 (2014) 1441-1443. https://doi.org/10.2217/nnm.14.91.
[63] M.L. Immordino, F. Dosio, L. Cattel, Stealth liposomes: Review of the basic science, rationale, and clinical applications, existing and potential, Int J Nanomedicine. 1 (2006) 297-315. 2426795
[64] M. Simard, M. Nedergaard, The neurobiology of glia in the context of water and ion homeostasis, Neuroscience. 129 (2004) 877-896. https://doi.org/10.1016/j.neuroscience.2004.09.053.
[65] M.V. Sofroniew, H.V. Vinters, Astrocytes: Biology and pathology, Acta Neuropathol. 119 (2010) 7-35. https://doi.org/10.1007/s00401-009-0619-8.
[66] M.L. Block, L. Zecca, J.S. Hong, Microglia-mediated neurotoxicity: Uncovering the molecular mechanisms, Nat Rev Neurosci. 8 (2007) 57-69. https://doi.org/10.1038/nrn2038.
[67] S.J. Soenen, E. Illyes, D. Vercauteren, K. Braeckmans, Z. Majer, S.C. De Smedt, M. De Cuyper, The role of nanoparticle concentration-dependent induction of cellular stress in the internalization of non-toxic cationic magnetoliposomes, Biomaterials. 30 (2009) 6803-6813.
https://doi.org/10.1016/j.biomaterials.2009.08.050.
[68] R. Banerjee, Liposomes: Applications in medicine, J Biomater Appl. 16 (2001) 3-21.
https://doi.org/10.1106/RA7U-1V9C-RV7C-8QXL.

[69] B. Fadeel, C. Bussy, S. Merino, E. Vazquez, E. Flahaut, F. Mouchet, L. Evariste, L. Gauthier, A.J. Koivisto, U. Vogel, C. Martin, L.G. Delogu, T. Buerki-Thurnherr, P. Wick, D. Beloin-Saint-Pierre, R. Hischier, M. Pelin, F. Candotto Carniel, M. Tretiach, F. Cesca, F. Benfenati, D. Scaini, L. Ballerini, K. Kostarelos, M. Prato, A. Bianco, Safety assessment of graphene-based materials: Focus on human health and the environment, ACS NANO. 12 (2018) 10582-10620. https://doi.org/10.1021/acsnano.8b04758.
[70] C. Bussy, H. Ali-Boucetta, K. Kostarelos, Safety considerations for graphene: Lessons learnt from carbon nanotubes, Acc Chem Res. 46 (2013) 692-701. 10.1021/ar300199e.
[71] M. Rezazadeh Azari, Y. Mohammadian, Comparing in vitro cytotoxicity of graphite, short multi-walled carbon nanotubes, and long multi-walled carbon nanotubes, Environ Sci Pollut Res Int. (2020). 10.1007/s11356-020-08036-4.
[72] V. Georgakilas, N. Tagmatarchis, D. Pantarotto, A. Bianco, J.P. Briand, M. Prato, Amino acid functionalisation of water soluble carbon nanotubes, Chem Commun (Camb). (2002) 3050-3051. https://doi.org/10.1039/b209843a.
[73] S. Li, W. Wu, S. Campidelli, V. Sarnatskaïa, M. Prato, A. Tridon, A. Nikolaev, V. Nikolaev, A. Bianco, E. Snezhkova, Adsorption of carbon nanotubes on active carbon microparticles, Carbon. 46 (2008) 1091-1095. https://doi.org/10.1016/j.carbon.2008.03.010.
[74] N. Lozano, W.T. Al-Jamal, A. Taruttis, N. Beziere, N.C. Burton, J. Van den Bossche, M. Mazza, E. Herzog, V. Ntziachristos, K. Kostarelos, Liposome-gold nanorod hybrids for high-resolution visualization deep in tissues, J Am Chem Soc. 134 (2012) 13256-13258. https://doi.org/10.1021/ja304499q.
[75] E. Kaiser, R.L. Colescott, C.D. Bossinger, P.I. Cook, Color test for detection of free terminal amino groups in the solid-phase synthesis of peptides, Anal Biochem. 34 (1970) 595-598. 10.1016/0003-2697(70)90146-6.
[76] G. Paxinos, K. Franklin, Paxinos and franklin's the mouse brain in stereotaxic coordinates, ed, 2012
[77] K.J. Livak, T.D. Schmittgen, Analysis of relative gene expression data using real-time quantitative pcr and the 2(-delta delta c(t)) method, Methods. 25 (2001) 402-408. https://doi.org/10.1006/meth.2001.1262.
[78] H. Dou, K. Birusingh, J. Faraci, S. Gorantla, L.Y. Poluektova, S.B. Maggirwar, S. Dewhurst, H.A. Gelbard, H.E. Gendelman, Neuroprotective activities of sodium valproate in a murine model of human immunodeficiency virus-1 encephalitis, J Neurosci. 23 (2003) 9162-9170. https://doi.org/10.1523/JNEUROSCI.23-27-09162.2003.
[79] H. Dou, J. Morehead, J. Bradley, S. Gorantla, B. Ellison, J. Kingsley, L.M. Smith, W. Chao, G. Bentsman, D.J. Volsky, H.E. Gendelman, Neuropathologic and neuroinflammatory activities of hiv-1-infected human astrocytes in murine brain, Glia. 54 (2006) 81-93. https://doi.org/10.1002/glia.20358.
[80] A.C. Ferraz, L.L. Xavier, S. Hernandes, M. Sulzbach, G.G. Viola, J.A. Anselmo-Franci, M. Achaval, C. Da Cunha, Failure of estrogen to protect the substantia nigra pars compacta of female rats from lesion induced by 6-hydroxydopamine, Brain Res. 986 (2003) 200-205. https://doi.org/10.1016/s0006-8993(03)03198-6.
[81] L.L. Xavier, G.G. Viola, A.C. Ferraz, C. Da Cunha, J.M. Deonizio, C.A. Netto, M. Achaval, A simple and fast densitometric method for the analysis of tyrosine hydroxylase immunoreactivity in the substantia nigra pars compacta and in the ventral tegmental area, Brain Res Brain Res Protoc. 16 (2005) 58-64. https://doi.org/10.1016/j.brainresprot.2005.10.002.
[82] F.G. Martinez, E.E. Hermel, L.L. Xavier, G.G. Viola, J. Riboldi, A.A. Rasia-Filho, M. Achaval, Gonadal hormone regulation of glial fibrillary acidic protein immunoreactivity in the medial amygdala subnuclei across the estrous cycle and in castrated and treated female rats, Brain Res. 1108 (2006) 117-126. https://doi.org/10.1016/j.brainres.2006.06.014.
[83] L. Saur, P.P. Baptista, P.N. de Senna, M.F. Paim, P. do Nascimento, J. Ilha, P.B. Bagatini, M. Achaval, L.L. Xavier, Physical exercise increases gfap expression and induces morphological changes in hippocampal astrocytes, Brain Struct Funct. 219 (2014) 293-302. https://doi.org/10.1007/s00429-012-0500-8.

Figures

Figures are provided as an attached single pdf document.

Figure Captions

Figure 1: Experimental design scheme and TEM of the different nanomaterials tested. (**A**) Experimental design of the present study. After stereotactic administration of different nanomaterials, brains were collected at different time points. Molecular and cellular analyses were performed in the injection site and in nearby regions (anterior and posterior). (**B**) Transmission electron microscopy characterisation of the nanomaterials (aminated MWNTs, carboxylated MWNTs, GO, cationic and anionic liposomes) used in this work.

Figure 2: RT-qPCR analysis results obtained in the brain striatum injection site. (**A**) Gene expression levels of transcripts encoding pro-inflammatory cytokines, chemokines, and anti-inflammatory cytokines. The analysis was performed at 1 d, 2 d, and 7 d after injection of LPS, 5% dextrose, cationic or anionic liposomes (1 µg/µl), MWNT-NH_3^+ or ox-MWNT (0.5 µg/µl), or GO (0.5 µg/µl). (**B**) Heat map presenting the statistical analysis. All statistical differences are shown in heatmap colours comparing dextrose with all types of material injected. Mean ± SEM, *p<0.05, **p<0.01, ***p<0.001 ****p<0.0001 vs 5% dextrose.

Figure 3: Quantitative analysis of glial cell immunohistochemical staining performed in different brain regions; anterior to the injection site (**A**), the injection site (**B**) and a posterior site (**C**) nearby the injection site. Relative proportion of the area (mean per ROI) covered by microglial (CD11b-immunopositive) cells (***i***), or astrocytes (GFAP-immunopositive cells) (***ii***) and estimated number of neurons (NeuN-immunopositive cells) (***iii***) counted in ROI were performed in the site of injection and in the regions anterior and posterior at 2 d after administration of LPS, 5% dextrose (ipsilateral and contralateral sides), MWNT-NH_3^+or ox-MWNT or GO (0.5 and 1 µg/µl), or cationic and anionic liposomes (1 µg/µl). Mean ± SEM; p-values are in comparison to 5% dextrose samples. *p<0.05, **p<0.01, ****p<0.0001 vs 5% dextrose. Representative images of the different immunostainings are presented in Figures S5, S6, and S7.

Figure 4: Representative images of cleaved-caspase 3 immunohistochemical staining. The immunophenotyping of cleaved-caspase 3 positive elements (undergoing apoptosis) in the injection site (the striatum) and in the anterior region distant from the injection site and in the posterior region adjacent to the injection site obtained at 2 d after injection of LPS, 5% dextrose, GO, and cationic liposomes. Note that apoptotic elements were visible in the injection site of LPS and cationic liposomes, while apoptotic cells visible in the GO-injected brain were comparable to the vehicle control (5% dextrose).

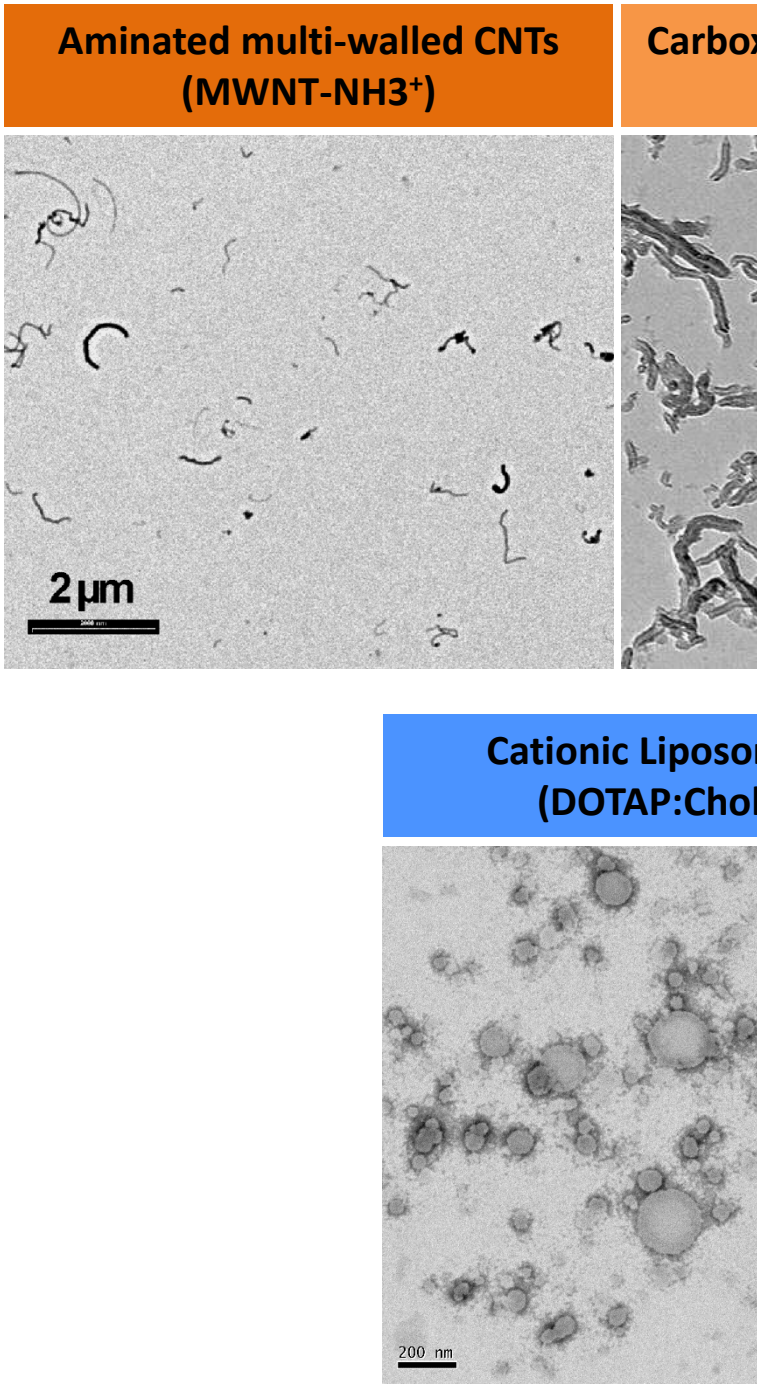
Aminated multi-walled CNTs
(MWNT-NH3+)
2 µm
Cationic Liposo
(DOTAP:Chol
200 nm

Figure 1

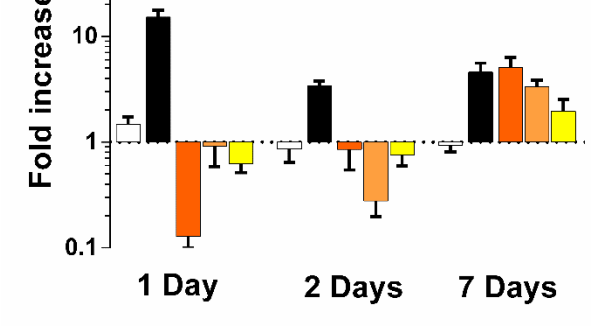
Ccl2
Fold increase
10
1
0.1
1 Day
2 Days
7 Days

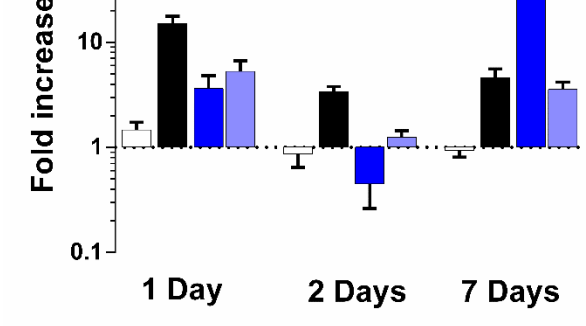
Fold increase
10
1
0.1
1 Day
2 Days
7 Days

B

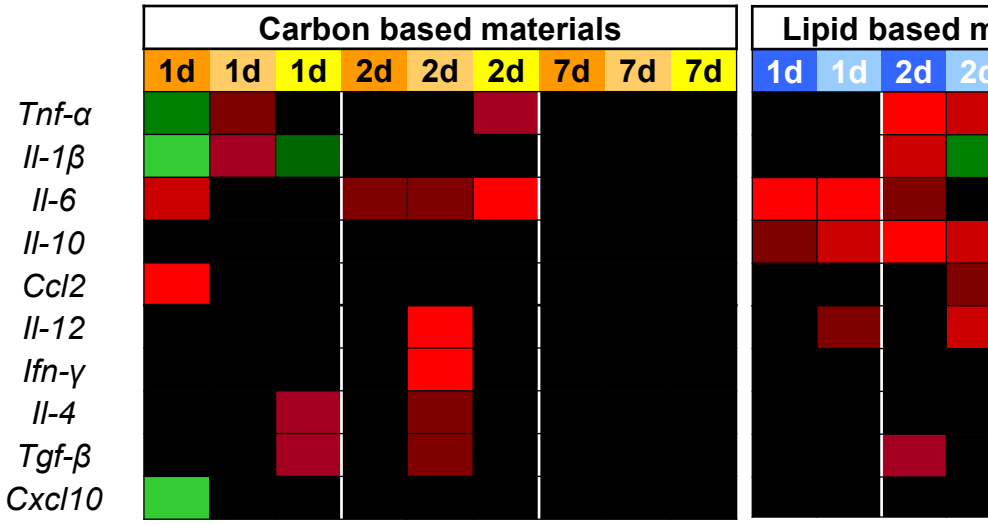
Carbon based materials
Lipid based m
1d
1d
1d
2d
2d
2d
7d
7d
7d
1d
1d
2d
Tnf-α
Il-1β
Il-6
Il-10
Ccl2
Il-12
Ifn-γ
Il-4
Tgf-β
Cxcl10

Figure 2

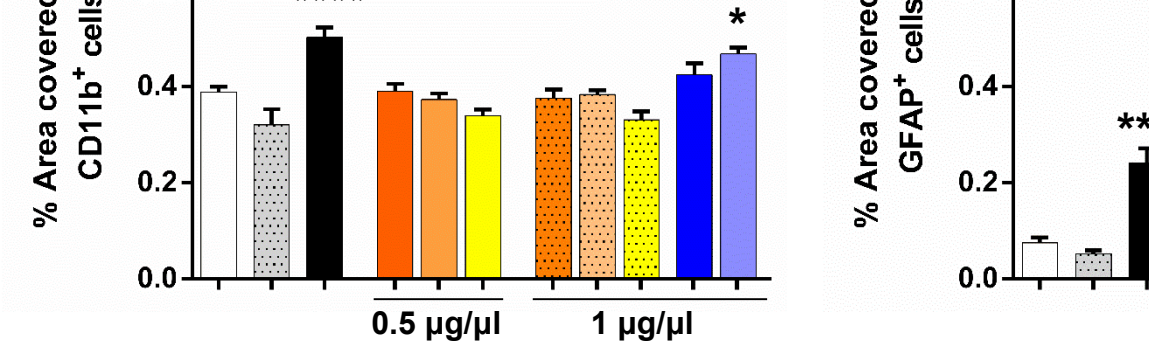
Posterior
% Area covered by CD11b+ cells
0.4
0.2
0.0
*
% Area covered by GFAP+ cells
0.4
0.2
0.0
**
0.5 µg/µl
1 µg/µl

Figure 3

Figure 4

Table of Content

Various nanomaterials are been explored for the brain delivery of therapeutic or imaging compounds. After administration in the brain, Portioli et al. demonstrate in a pilot study that functionalised carbon based nanomaterials may present a better safety profile than highly charged liposomes. Graphene Oxide nanosheets could even alleviate the inflammation caused by their direct injection in the brain.

Corinne Portioli, Cyrill Bussy, Mariarosa Mazza, Neus Lozano, Dhifaf A. Jasim, Maurizio Prato, Alberto Bianco, Marina Bentivoglio and Kostas Kostarelos

Injection of Graphene Oxide Nanosheets in the Brain Does not Induce Acute Neurotoxicity and Counteracts the Acute Microglial Activation related to Surgery in a Pilot Study

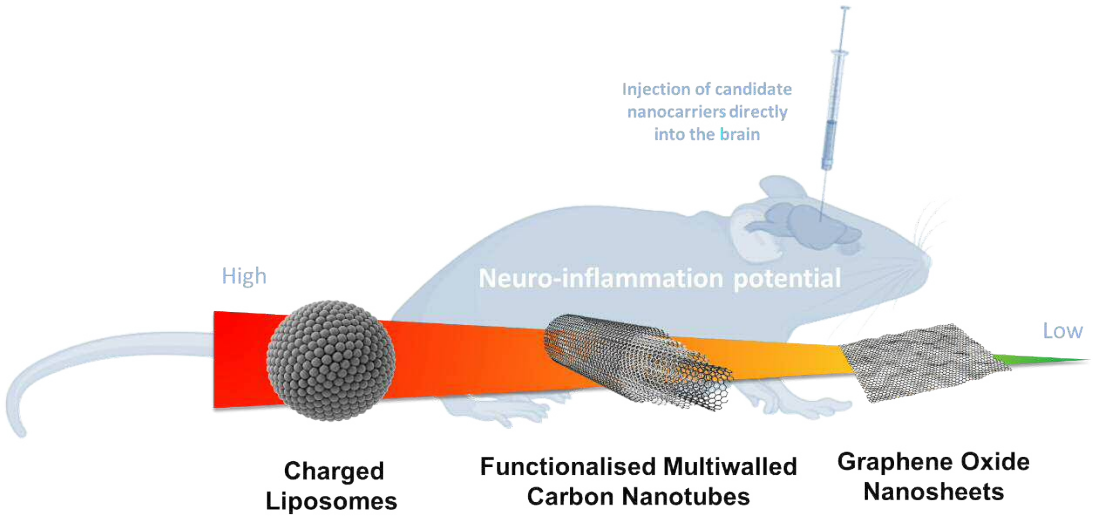

Supplementary Information

A supplementary information document with supplementary figures is provided as an attached single pdf document.

Supplementary Figure Captions

Table S1: Forward and reverse sequences of the primers used in the present study.

Table S2: Primary and secondary antibodies and solutions used for immunohistochemical procedures.

Figure S1: Material characteristics. The different material characteristics (length, amount of amination and oxidation, zeta-potential, lateral dimensions, polydispersity, and thickness) are presented for (**A**) *f*-MWNTs (MWNT-NH_3^+ and ox-MWNT), (*) this data was previously published in Bussy et al. Nanoscale 2016 (ref. 55 in this article), (**B**) GO sheets, and (**C**) liposomes (DOTAP:Chol and DOPG:Chol).

Figure S2: RT-qPCR analysis of gene expression levels in the brain region posterior to the injection site. (**A**) Gene expression levels of transcripts encoding pro-inflammatory cytokines, chemokines, and anti-inflammatory cytokines. The analysis was performed at 1 d, 2 d, and 7 d after injection of LPS, 5% dextrose, cationic or anionic liposomes (1 µg/µl), MWNT-NH_3^+or ox-MWNT (0.5 µg/µl), or GO (0.5 µg/µl). (**B**) Heat map presenting the statistical analysis. All statistical differences are shown in heat map colours comparing dextrose with all types of material injected. Mean ± SEM, *p<0.05, **p<0.01, ***p<0.001 ****p<0.0001 vs 5% dextrose.

Figure S3: RT-qPCR analysis of gene expression levels in the brain region anterior to the injection site. (**A**) Relative gene expression levels of transcripts encoding pro-inflammatory and anti-inflammatory cytokines and chemokines obtained at 1 d and 2 d after injection of LPS, 5% dextrose, cationic or anionic liposomes (1 µg/µl). (**B**) Heat map presenting the statistical analysis. All statistical differences are shown in heat map colours comparing dextrose with all types of material injected. Mean ± SEM, *p<0.05, **p<0.01, ***p<0.001 ****p<0.0001 vs 5% dextrose.

Figure S4: CD11b immunohistochemical staining of microglia. (**A**) Representative images of microglial cells as visualised by CD11b immunoreactivity in the three analysed brain regions (site of injection, anterior brain region distant from the site of injection, and posterior brain region adjacent to the site of injection) at 2 d after the injection of LPS, 5% dextrose, MWNT-NH_3^+ or ox-MWNT or GO (0.5 and 1 µg/µl), or cationic or anionic liposomes (1 µg/µl). (**B**) Densitometric evaluation (in optical density, or OD units) of the CD11b immunosignal intensity is shown in the injection site at 2 d after

the administration of LPS, 5% dextrose, GO (0.5 and 1 µg/µl), or cationic or anionic liposomes (1 µg/µl). Mean ± SEM; the p-value is for the comparison with 5% dextrose samples: *p<0.05, **p<0.01.

Figure S5: GFAP immunohistochemical staining of astrocytes. (**A**) Representative images of astrocytes as visualised by GFAP immunoreactivity in the three analysed brain regions (site of injection, anterior brain region to site of injection, and posterior brain region to site of injection) at 2 d after the injection of LPS, 5% dextrose, MWNT-NH_3^+or ox-MWNT or GO (0.5 and 1 µg/µl), or cationic or anionic liposomes (1 µg/µl). (**B**) Estimated number of astrocytes (per ROI) counted stereologically at the site of injection and in the regions anterior and posterior is shown at 2 d after injection of LPS, 5% dextrose, or cationic liposomes. Mean ± SEM; the p value is for to the comparison with 5% dextrose samples: ***p<0.001.

Figure S6: NeuN immunohistochemical staining of neurons. Representative images of neuronal cells as visualised by NeuN immunoreactivity in the three analysed brain regions (site of injection, anterior brain region to site of injection and posterior brain region to site of injection) at 2 d after the injection of LPS, 5% dextrose, MWNT-NH_3^+or ox-MWNT or GO (0.5 and 1 µg/µl), or cationic or anionic liposomes (1 µg/µl). Quantitative evaluation of this staining is presented in Figure 3.

Figure S7: **FluoroJade B staining.** Representative images of Fluoro-Jade B staining in the cerebral cortex and in the striatum regions of the coronal brain sections containing the injection site at 2 d after administration of LPS, 5% dextrose, GO, or cationic liposomes. Degenerating neurons, labelled by green Fluoro-Jade B fluorescent staining, were visible mainly in the LPS- (cortex around the needle track and striatum) and cationic liposome (striatum)-treated tissues.

Supplementary Information
(Tables and Figures)

Injection of Graphene Oxide Nanosheets in the Brain Does not Induce Acute Neurotoxicity and Counteracts the Acute Microglial Activation related to Surgery in a Pilot Study

Corinne Portioli[1, 2, $], Cyrill Bussy[1, 3, 4 *], Mariarosa Mazza[1], Neus Lozano[1, 3], Dhifaf A. Jasim[1,3], Maurizio Prato[5,6], Alberto Bianco[7], Marina Bentivoglio[2] and Kostas Kostarelos[1,3,8, *, &]

[1] Nanomedicine Lab, School of Health Sciences, Faculty of Biology, Medicine & Health, The University of Manchester, Manchester Academic Health Science Centre, Manchester, UK

[2] Department of Neurosciences, Biomedicine and Movement Sciences, University of Verona, Verona, Italy

[3] National Graphene Institute, The University of Manchester, Manchester, UK

[4] Lydia Becker Institute of Immunology and Inflammation, Faculty of Biology, Medicine and Health, The University of Manchester, Manchester Academic Health Science Centre, Manchester, UK

[5] Department of Chemical and Pharmaceutical Sciences, University of Trieste, 34127 Trieste, Italy

[6] Carbon Nanobiotechnology Laboratory, CIC BiomaGUNE, 20009 San Sebastian, Spain.

[7] University of Strasbourg, CNRS, Immunology, Immunopathology and Therapeutic Chemistry, UPR 3572, Strasbourg, France

[8] Catalan Institute of Nanoscience and Nanotechnology (ICN2), and The Barcelona Institute of Science and Technology (BIST), Campus UAB, Bellaterra, Barcelona, Spain

Table S1: Forward and reverse sequences of the primers used in the present study.

Gene	Forward sequence (5'-3')	Reverse sequence (5'-3')
mβ-actin	GACCTCTATGCCAACACAGT	AGTACTTGCGCTCAGGAGGA
mTNFα	CAGACCCTCACACTCAGATCATCT	CCTCCACTTGGTGGTTTGCTA
mIL-1β	GGACAGAATATCAACCAACAAGTGATA	GTGTGCCGTCTTTCATTACACAG
mIL-6	ATGGATGCTACCAAACTGGA	CCTCTTGGTTGAAGATATGA
mIL-12	AGAGGTGGACTGGACTCCCG	AGTCTCGCCTCCTTTGTGGC
mINFγ	TCAAGTGGCATAGATGTGGAAGAA	TGGCTCTGCAGGATTTTCATG
mCXCL10	GACGGTCCGCTGCAACTG	GCTTCCCTATGGCCCTCATT
mCCL2	CATGCTTCTGGGCCTGCTGTTC	CCTGCTGCTGGTGATCCTCTTGTAG
mIL-10	GGTTGCCAAGCCTTATCGGA	ACCTGCTCCACTGCCTTGCT
mTGFβ	GACCAGCCGCCGCCGCAGG	AGGGCTGTCTGGAGTCCTC
mIL-4	GAGACTCTTTCGGCTTTTC	TGATGCTCTTTAGGCTTTCCA

Table S2: Primary and secondary antibodies and solutions used for immunohistochemical procedures.

Marker	Pre-incubation	Primary antibody	Dilution	Supplier	Secondar antibody	Dilution
Neurons	normal horse serum 5%	mouse anti-NeuN	1:500	Millipore, Massachusetts, US	biotinylated horse anti-mouse	1:200
Astrocytes	normal goat serum 5%	rabbit polyclonal anti-GFAP	1:500	Dako, Carpinteria, US	biotinylated goat anti-rabbit	1:200
Microglial cells	normal goat serum 5%	rat anti-CD11b	1:500	AbD Serotec, Oxford, UK	biotinylated goat anti-rat	1:200
Apoptotic cells	normal horse serum 5%	rabbit anti-cleaved caspase 3 (Asp175)	1:600	Cell Signaling, Danvers, US	biotinylated horse anti-rabbit	1:200

A

Measurement	Aminated multi-walled CNTs ($MWNT\text{-}NH_3^+$) cycloaddition	Carboxylated multi-walled CNTs (Ox-MWNT) acidic treatment
Length (TEM)	500 – 2000 nm	200 – 300 nm
Diameter (TEM)	20 - 30 nm	20 - 30 nm
Amount of amination (Kaiser test)	58 µmol/g	-
Amount of carboxyl groups (TGA)	-	1,7 µmol/g (*)

B

Measurement	Graphene Oxide Sheets (GO)
Zeta potential	-50.0 ± 0.4 mV
Lateral dimensions (TEM)	10 – 1800 nm
Thickness (AFM)	0.9 - 4.8 nm

C

Measurement	Cationic Liposomes, DOTAP:Chol (2:1)	Anionic Liposomes, DOPG:Chol (2:1)
	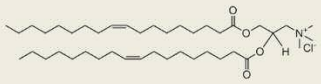	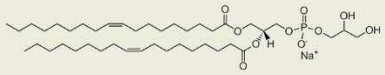
Zeta potential	- 54.1 ± 0.5 mV	+ 60.5 ± 2.6 mV
Hydrodynamic diameter (DLS)	118.1 ± 3.0 nm	125.6 ± 2.6 nm
Polydispersity	0.329 ± 0.022	0.250 ± 0.007

Figure S1: Material characteristics. The different material characteristics (length, amount of amination and oxidation, zeta-potential, lateral dimensions, polydispersity, and thickness) are presented for (**A**) *f*-MWNTs ($MWNT\text{-}NH_3^+$ and ox-MWNT), (*) this data was previously published in Bussy et al. Nanoscale 2016 (ref. 55 in this article), (**B**) GO sheets, and (**C**) liposomes (DOTAP:Chol and DOPG:Chol).

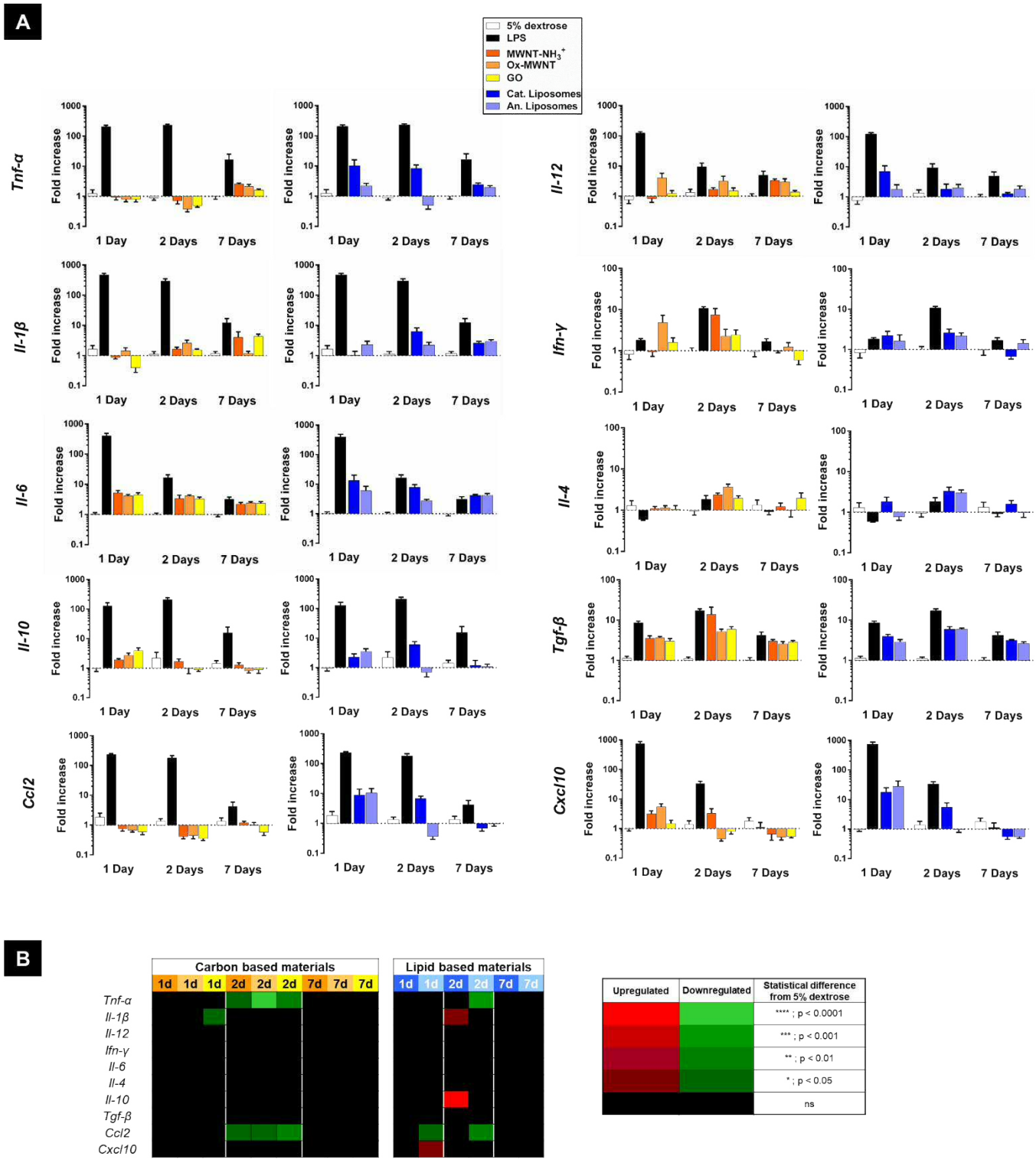

Figure S2: RT-qPCR analysis of gene expression levels in the brain region posterior to the injection site. (**A**) Gene expression levels of transcripts encoding pro-inflammatory cytokines, chemokines, and anti-inflammatory cytokines. The analysis was performed at 1 d, 2 d, and 7 d after injection of LPS, 5% dextrose, cationic or anionic liposomes (1 µg/µl), MWNT-NH_3^+or ox-MWNT (0.5 µg/µl), or GO (0.5 µg/µl). (**B**) Heat map presenting the statistical analysis. All statistical differences are shown in heat map colours comparing dextrose with all types of material injected. Mean ± SEM, *p<0.05, **p<0.01, ***p<0.001 ****p<0.0001 vs 5% dextrose.

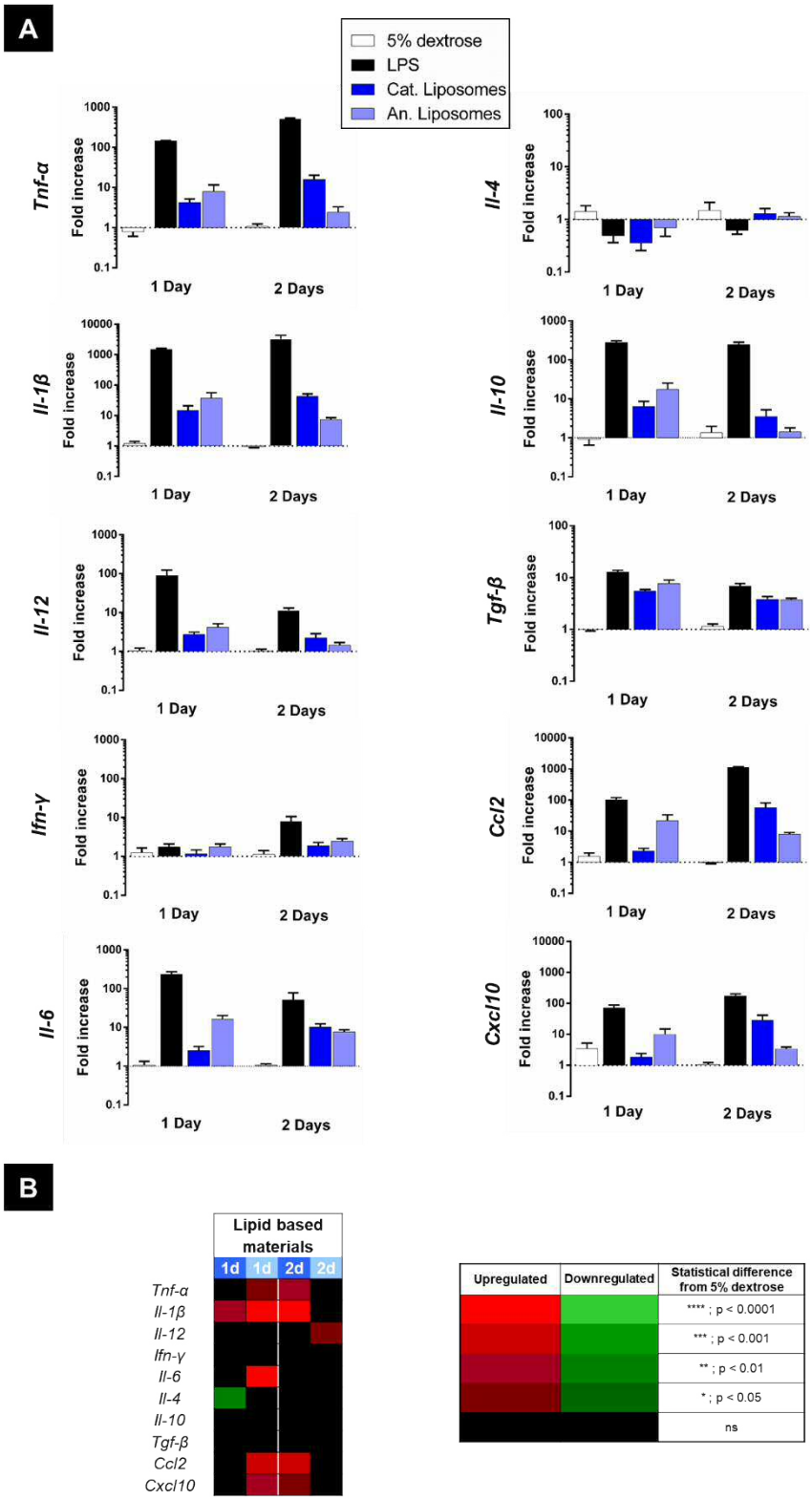

Figure S3: RT-qPCR analysis of gene expression levels in the brain region anterior to the injection site. (**A**) Relative gene expression levels of transcripts encoding pro-inflammatory and anti-inflammatory cytokines and chemokines obtained at 1 d and 2 d after injection of LPS, 5% dextrose, cationic or anionic liposomes (1 µg/µl). (**B**) Heat map presenting the statistical analysis. All statistical differences are shown in heat map colours comparing dextrose with all types of material injected. Mean ± SEM, *p<0.05, **p<0.01, ***p<0.001 ****p<0.0001 vs 5% dextrose.

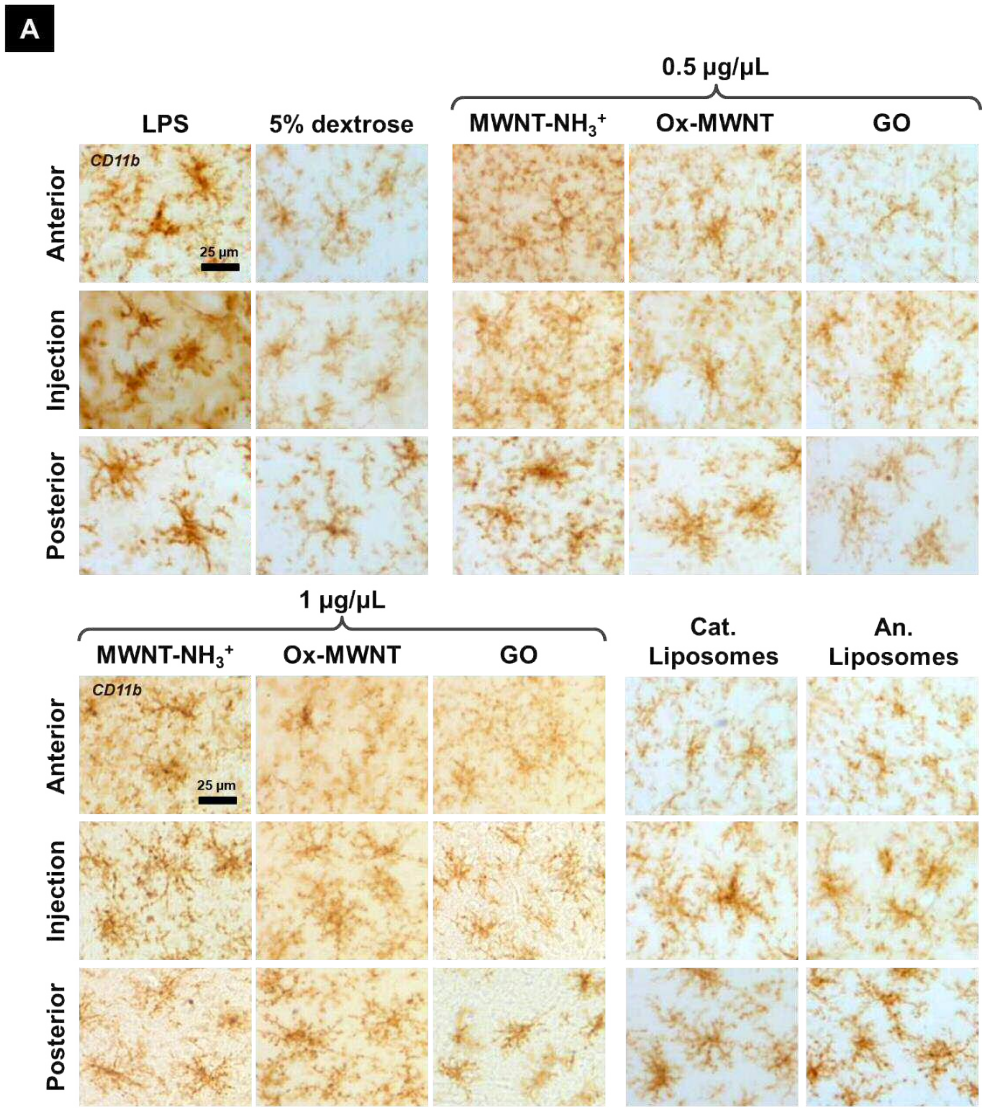

Figure S4: CD11b immunohistochemical staining of microglia. (**A**) Representative images of microglial cells as visualised by CD11b immunoreactivity in the three analysed brain regions (site of injection, anterior brain region distant from the site of injection, and posterior brain region adjacent to the site of injection) at 2 d after the injection of LPS, 5% dextrose, MWNT-NH_3^+ or ox-MWNT or GO (0.5 and 1 µg/µl), or cationic or anionic liposomes (1 µg/µl). (**B**) Densitometric evaluation (in optical density, or OD units) of the CD11b immunosignal intensity is shown in the injection site at 2 d after the administration of LPS, 5% dextrose, GO (0.5 and 1 µg/µl), or cationic or anionic liposomes (1 µg/µl). Mean ± SEM; the p-value is for the comparison with 5% dextrose samples: *p<0.05, **p<0.01.

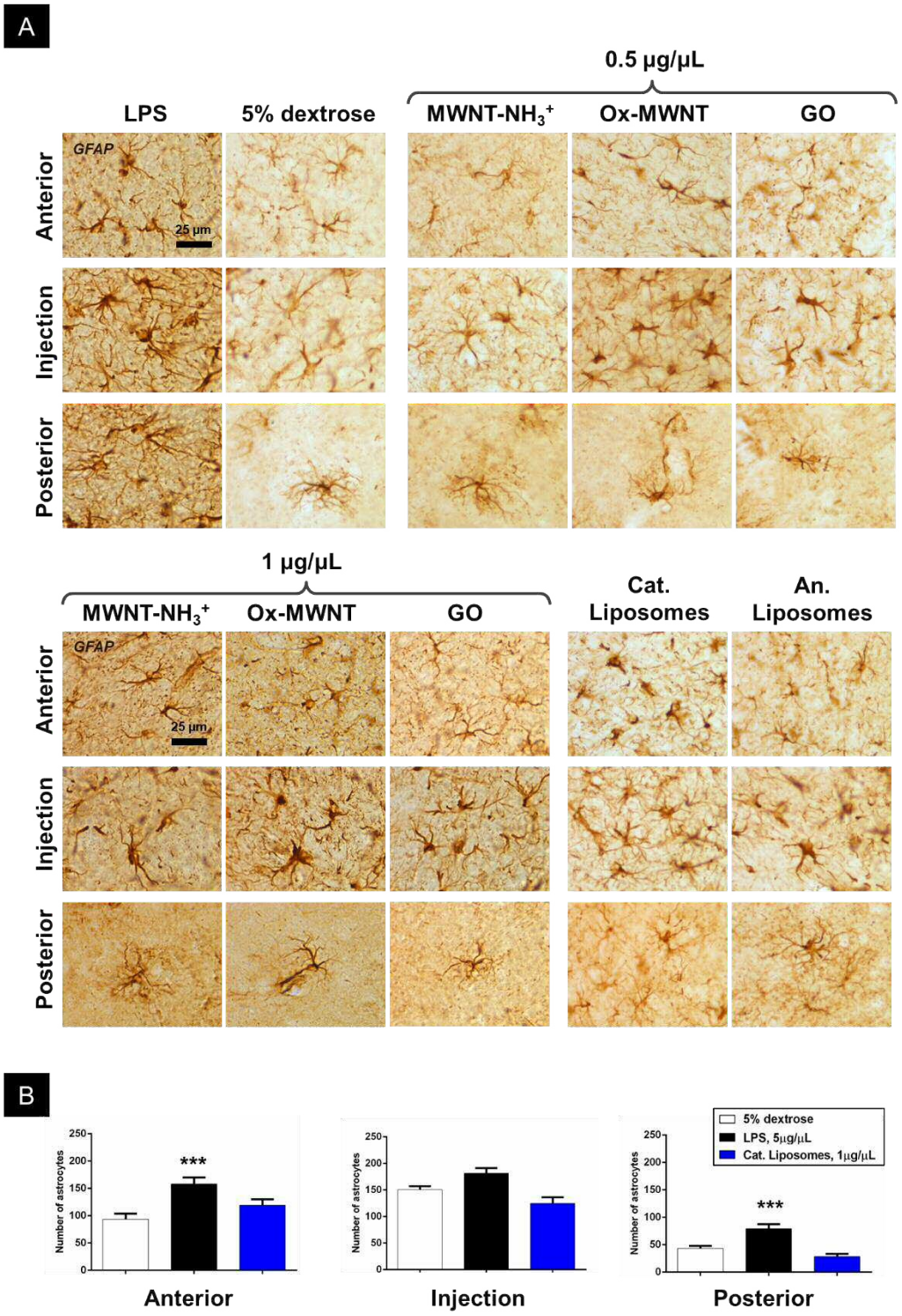

Figure S5: GFAP immunohistochemical staining of astrocytes. (**A**) Representative images of astrocytes as visualised by GFAP immunoreactivity in the three analysed brain regions (site of injection, anterior brain region to site of injection, and posterior brain region to site of injection) at 2 d after the injection of LPS, 5% dextrose, MWNT-NH_3^+or ox-MWNT or GO (0.5 and 1 µg/µl), or cationic or anionic liposomes (1 µg/µl). (**B**) Estimated number of astrocytes (per ROI) counted stereologically at the site of injection and in the regions anterior and posterior is shown at 2 d after injection of LPS, 5% dextrose, or cationic liposomes. Mean ± SEM; the p value is for to the comparison with 5% dextrose samples: ***p<0.001.

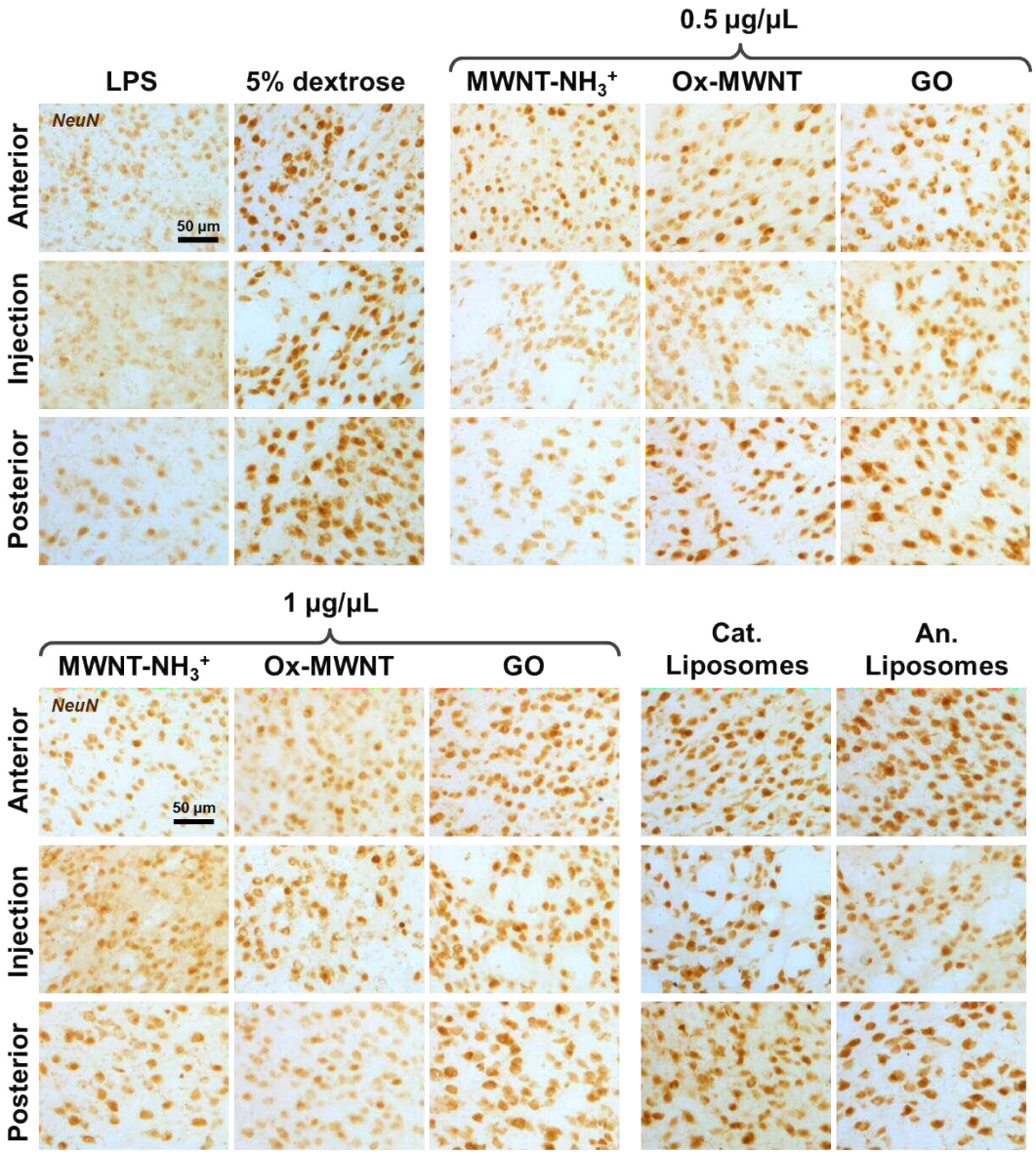

Figure S6: NeuN immunohistochemical staining of neurons. Representative images of neuronal cells as visualised by NeuN immunoreactivity in the three analysed brain regions (site of injection, anterior brain region to site of injection and posterior brain region to site of injection) at 2 d after the injection of LPS, 5% dextrose, MWNT-NH_3^+or ox-MWNT or GO (0.5 and 1 µg/µl), or cationic or anionic liposomes (1 µg/µl). Quantitative evaluation of this staining is presented in Figure 3.

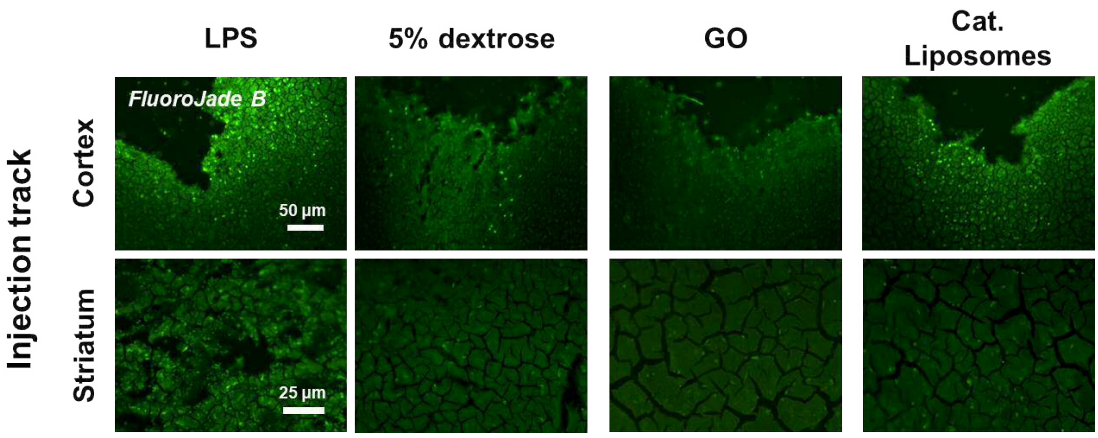

Figure S7: **FluoroJade B staining.** Representative images of Fluoro-Jade B staining in the cerebral cortex and in the striatum regions of the coronal brain sections containing the injection site at 2 d after administration of LPS, 5% dextrose, GO, or cationic liposomes. Degenerating neurons, labelled by green Fluoro-Jade B fluorescent staining, were visible mainly in the LPS- (cortex around the needle track and striatum) and cationic liposome (striatum)-treated tissues.

Click here to access/download

Supporting Information

Portioli et al_SMALL_supp info_07092020.docx

all figures as pdf format

Click here to access/download

Production Data

Portioli et al _all figures included_SMALL_prod file.pdf

supporting information file as word doc

Click here to access/download

Production Data

Portioli et al_supp info_SMALL_07092020.docx

main figures as pdf format

Click here to access/download

Production Data

Portioli_et al _all main figures_SMALL_07092020.pdf

main text word clean

Click here to access/download

Production Data

Portioli et al_text _SMALL_09102020 R2_clean.docx